Politecnico di Torino

Corso di Laurea Magistrale
In Ingegneria Energetica e Nucleare
A.a. 2021/2022
Sessione di Laurea ottobre 2022

Experimental qualification of the first DTT TF superconducting cables in SULTAN

Relatori:
Prof. Roberto Bonifetto
Dr. Andrea Zappatore

Candidato:
Giuseppe Scarantino

Contents

Abstract

The objective of this work is the experimental qualification of the performance of the first ENEA superconducting (SC) cables for the toroidal-field (TF) coils of the Divertor Tokamak Test (DTT) Facility that is being built in Frascati [1]. Two full-scale, short-length conductor samples with different twist-pitch have been tested from the begin of July 2022 in SULTAN, a test facility operated by EPFL-SPC (Swiss Plasma Center) and located at Paul Scherrer Institute (PSI) in Villigen, Switzerland. In this one-of-a-kind magnetic facility, the superconductors have been tested in a forced flow of supercritical Helium with nominal current and magnetic field up to 11 T. Before testing, the SC cables made of Nb_3Sn were prepared in the facility: they underwent heat-treatment and were assembled and instrumented with high precision thermometers, voltage taps and, in the case of one of the two samples (the TF-B one), also equipped with pressure capillaries to allow a more precise hydraulic characterization. In the three-week test campaign, hydraulic tests and power tests (both DC and AC) with current and field were carried out to assess the performance of the SC samples. The main performance parameters for a SC magnet were investigated in specific tests: experiments on critical current and current sharing temperature (DC tests), minimum quench energy MQE tests and AC loss measurements. Applying cyclic electromagnetic loads to the sample, the performance degradation after cycles was investigated, measuring periodically the current sharing temperature and analyzing the broadness of the transition to the normal conducting state. Also, the degradation after two thermal cycles (warm-up and cool-down) were assessed. The measurements of current sharing temperature at different EM loading conditions (i.e., different current and applied field) were also carried out, allowing the analysis of the cable strain under different Lorentz forces.

The important results emerged from the detailed analysis of the tests of the first two TF samples (hydraulic characterization, DC and AC tests) are reported in this thesis.

1. Introduction

1.1 Introduction to Superconductivity

Superconductivity is the quantum phenomenon of zero electrical resistivity and perfect diamagnetism exhibited by certain materials when cooled below their critical temperature T_c, are exposed to a magnetic field below the critical one B_c, and carry a current not exceeding the critical current density J_c [2]. The range of these three parameters defines the so-called critical surface, below which the materials are superconducting (Figure 1.1.1). Above the critical surface, the material transits to a normal conducting state and dissipates energy by Ohmic heating when carrying a current. In present applications, superconductors are used for their high magnetic field generation, rather than their high current-carrying capabilities (Figure 1.1.2). Thus, they are used as superconducting magnets. In several fields, from commercial magnetic resonance imaging to high energy physics and thermonuclear fusion, superconducting magnets are a key technology.

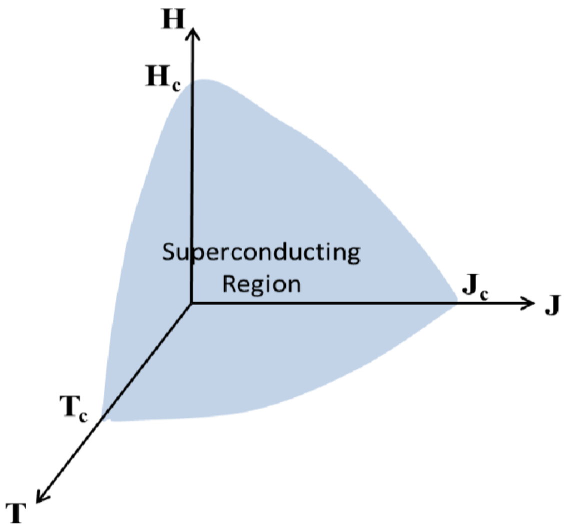

Figure 1.1.1: Schematic representation of the critical surface of a superconductor [55].

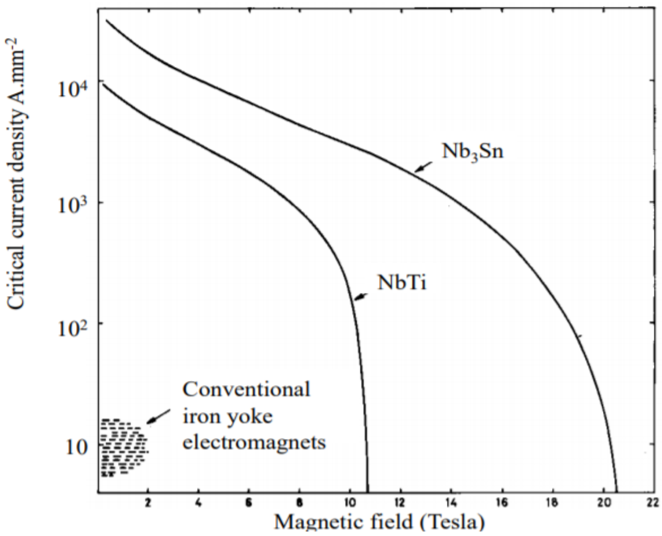

Figure 1.1.2: Comparison of the ranges in magnetic field generated by conventional electromagnets and NbTi, Nb3Sn superconductors [30].

In present applications, the most established superconducting materials are Nb-based metal composites, the NbTi and Nb_3Sn, belonging to the category of Low Temperature Superconductors (LTS) for their critical temperature lower than 20 K.

These are practically used at a temperature around 4.5 K to benefit of the highest performance (i.e., highest field and temperature margin). The other category of superconductors discovered more recently is that of High Temperature Superconductors (HTS), which are materials based on copper oxides (cuprates: BSCCO or ReBCOs [3]) or some iron-based compounds (pnictides/chalcogenides [4]). The copper-oxides-based HTS are currently opening a new era of superconducting magnets, increasing their interest and research efforts in the fields of Thermonuclear Fusion and High Energy Physics. The possibility to generate stronger magnetic fields in an even more compact configuration with higher operating temperature, and higher temperature span over which the magnet remains superconducting, are some of the reasons that keep such interest on these materials (Figure 1.1.4). However, due to still open technological challenges, some of the new planned projects in the nuclear fusion field still employ the well-established Low Temperature Superconductors. This is the case, for instance, of the ITER, DTT, and even DEMO reactors.

Figure 1.1.3: Example of LTS (NbTi, Nb3Sn) wires, cables and tapes manufactured by LUVATA® [56].

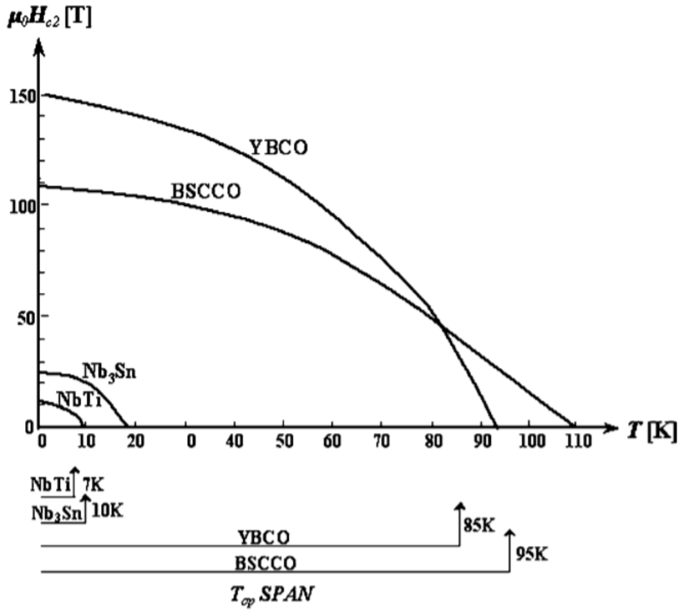

Figure 1.1.4: Inductive field vs. T plots for low temperature superconductors (NbTi and Nb3Sn) and high temperature superconductors (BSCCO and YBCO) [57].

1.2 Superconductivity and Nuclear Fusion

In a thermonuclear fusion reactor, the collision of two light nuclei results in the formation of other nuclei and subatomic particles. Energy is produced from the reaction due to the conversion of part of the mass of the reactants into kinetic energy of the products. The conversion of this into heat and electricity in a continuous and reliable way is at the base of the future fusion power plants. To make possible this type of reaction (i.e., fusion reaction) the reagent nuclei must be kept at temperatures of the order of millions of Celsius degrees, to overcome the coulomb repulsion between the two positively charged nuclei. In Figure 1.2.1 is shown the cross-section (i.e., the probability of occurrence) of some of the known fusion reactions, as a function of kinetic energy (i.e., temperature). The reaction that appears to be the most promising is the DT reaction (Deuterium-Tritium). It shows the lowest value of minimum energy (lowest activation temperature), and it has the highest reaction rate (cross-section) compared to the other reactions in the range of the technologically achievable temperatures (~500 keV) [5]. These values of energies (temperature) correspond to millions of Kelvins, being 1 eV (*elettronvolt*) ~10^4 K as order of magnitude, meaning that even for a DT reaction the fuel must be maintained at about 150 million °C, which is a value impossible to withstand for any material.

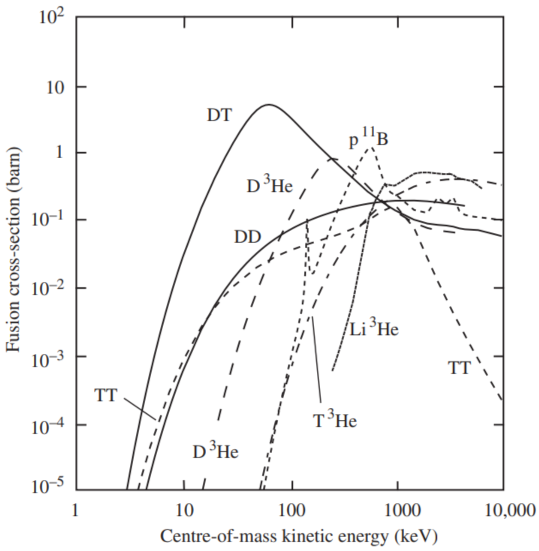

Figure 1.2.1: Fusion cross sections versus center-of-mass energy for reactions of interest to controlled fusion energy [6].

Having to manage such extreme temperatures, different technological solutions have been studied. Among these, the most promising idea is to take advantage of the state of plasma of the fuel at these temperatures (i.e., strongly ionized gas), and employ strong magnetic fields to confine it inside the reactor. This is the core idea behind the magnetic confinement fusion reactors and makes the link between thermonuclear fusion and superconducting magnets. Considering the necessity to generate high magnetic fields, and the final goal of electrical power production behind the research in fusion, superconducting magnets are an enabling technology [7]. They represent either the most cost-effective or the only feasible way to generate DC magnetic fields (> 2 T) in large volumes (>10 cm^3), reducing both the capital expense and the cost of operation with respect to conventional magnet systems [8].

Based on the magnetic confinement scheme, several major types of fusion reactor concepts can be distinguished, but the two most important are the Tokamak and the Stellarator. Tokamaks are the most diffused and are believed to represent the most promising option. In a Tokamak, the magnetic field to confine the plasma inside the vacuum vessel is the result of three main magnet systems generating directly or inductively the necessary magnetic field components. These are the Central Solenoid (CS), the Toroidal Field coils (TF) and the Poloidal Field coils (Figure 1.2.2). The Central Solenoid is operated in varying current regime. It acts as the primary circuit of a transformer, inducing a toroidal current in the plasma. This plasma current creates one of the components of the resulting magnetic field. The D-shaped Toroidal Field coils are the only magnets operated in DC to generate another field component parallel to the plasma current, while the Poloidal Field coils adds vertical field components which are fundamental for the vertical stability of the plasma. The resulting helical-shaped magnetic field guarantees the plasma confinement for a specific *confinement period*, depending on the period of discharge of the Central Solenoid. Based on this inductive mechanism, Tokamaks are pulsed machines.

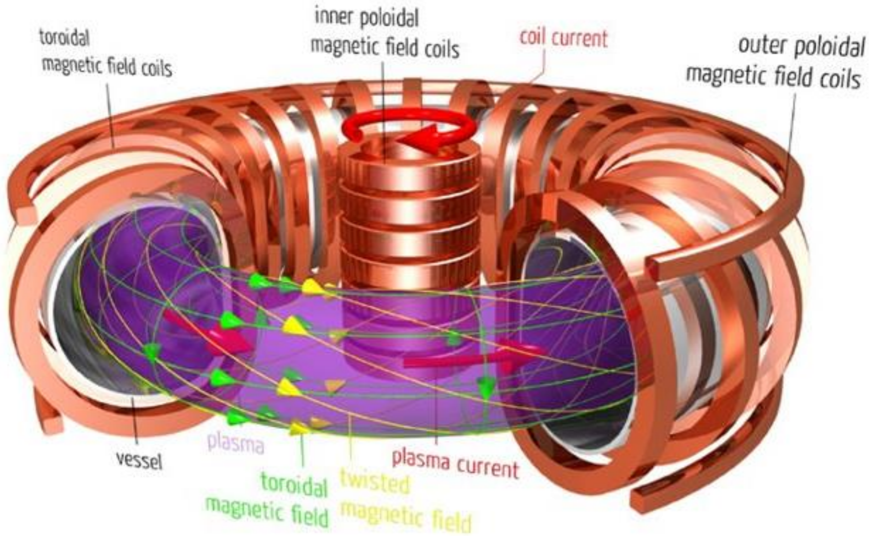

Figure 1.2.2: Schematic representation of a Tokamak with evidence on the magnet system components [9].

Superconducting magnets are already employed in several large-scale fusion devices around the world, either in operation or under construction. For example, JT-60SA, KSTAR, EAST, Tore Supra, W7-X are some of the reactors already in operation. The biggest and most ambitious project for the scale, purposes, international involvements, and financial efforts is the ITER project, currently under construction and foreseen to start its operation by the end of 2025. ITER (acronym of International Thermonuclear Experimental Reactor) aims at demonstrating the feasibility of thermonuclear fusion as an energy source. It is expected to produce 500 MW of thermal fusion power, with an aimed power gain (the “Q factor”) of about 10. It will be the first fusion device to test the integrated technologies, materials, and physics regimes necessary for the commercial production of fusion-based electricity [10]. Beyond ITER, the next step would be the construction of demonstrators: fusion reactor prototypes able to demonstrate the reliable production of electricity. One of such prototypes is the European DEMO, a machine that will be designed within the EUROfusion consortium.

In the challenge for humanity towards the use of thermonuclear fusion as an energy source, many efforts must be devoted in the research and development of all the fundamental technologies. Among these, one of the biggest challenges is the superconducting magnet system. R&D is needed to optimize it, reducing the cost which still drives the capital cost of fusion devices.

1.3 The Divertor Tokamak Test Facility and Magnet System

In the asset of the European fusion community mission towards fusion electricity, other research facilities will be built in the forthcoming years to accelerate the research, testing alternative strategies from the ones developed in ITER, if for instance some of the designed technologies showed criticalities towards the extrapolation to DEMO. On such path, the Divertor Tokamak Test (DTT) facility will test alternative solutions to the problem of the plasma power-exhaust. In this facility, promising alternative concepts for the heat-exhaust system (called *divertor*) will be implemented and tested.

DTT is a superconducting (SC) tokamak currently under construction at the ENEA research center in Frascati, Rome. It has been designed to achieve plasma conditions of interest following the EUROfusion targets. The relatively high toroidal field (B_T = 6 T) will give the possibility to achieve plasma performances (mainly measured by the ratio between power and major radius of about 15 MW/m), not far from those in DEMO. The main design and operational parameters for DTT compared to ITER and DEMO are reported in Table 1.

	DTT	ITER	DEMO
R (m)	**2.19**	6.2	9.1
a (m)	**0.7**	2	2.93
A	**3.1**	3.1	3.1
I_p (MA)	**5.5**	15	19.6
B (T)	**6**	5.3	5.7
Heating P_{tot} (MW)	**45**	120	460
P_{sep} /R (MW/m)	**15**	14	17
Pulse length (s)	**95**	400	7600

Table 1: Comparison among DTT, ITER and DEMO [1].

The magnet system of DTT (Figure 1.3.1) is based on three groups of superconducting coils: 18 Toroidal Field coils (TFCs), providing a magnetic field of 6.0 T on the plasma axis (radial distance of $2.14\ m$); 6 external Poloidal Field (PF) coils, providing plasma shaping and stabilization; a stack of 6 identical modules for the Central Solenoid (CS) which are independently fed [11]. To cope with the foreseen performances, the TF, the CS and PF1&6 coils have been designed using Nb_3Sn strands, whereas the other 4 PF coils rely on NbTi, as they work at lower magnetic field values. The technology of Cable-In-Conduit Conductors (CICCs), cooled down by a forced flow of supercritical He gas having an inlet temperature of 4.5 K, guarantees intrinsic high structural capability [11].

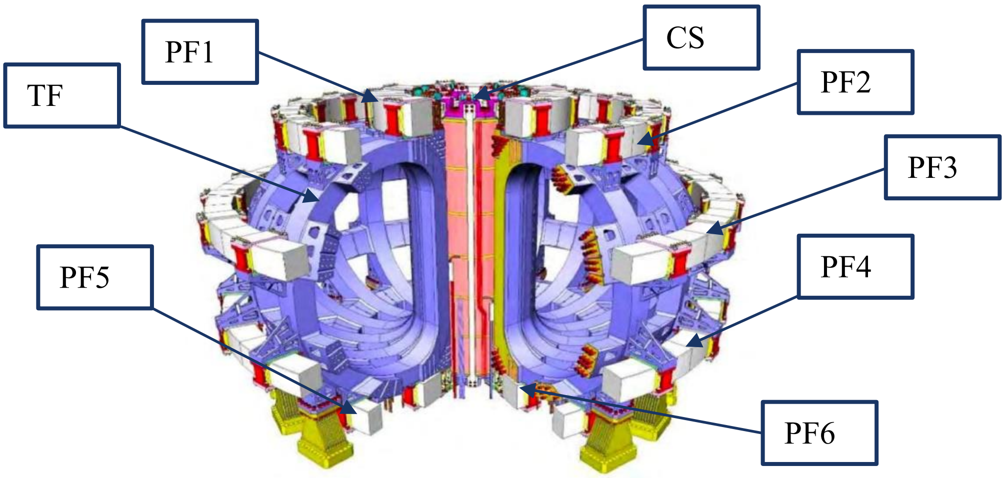

Figure 1.3.1: The DTT superconducting magnet system [33].

The Cable-In-Conduit configuration is the leading technology in LTS superconductors for fusion applications. Superconducting filaments having diameter of the order of ~10 um, are arranged in a ~1 mm thick wire with a copper matrix, necessary to give the structural, thermal, and electrical stability. To form the cable, several strands are twisted in one or multiple stages. Sometimes, a pressure relief channel is placed between the strands (usually in the middle of the cable), this lowers the pressure drop of the supercritical Helium flowing inside the conductor, improving the cooling. The twisting of the cable is fundamental to lower the coil inductance, important for the charge, discharge, and safety of the magnet [8].

The inductance unbalance inside a cable can be dangerous because of the favoring of coupling currents which deposit power in the cable (AC losses). Also, this unbalance can increase the risk that some strands hit the critical surface by carrying more current than the others, generating and propagating what is commonly called a quench (i.e., the transition to a normal conducting state). The cable in the CICC configuration is externally composed by a solid steel structure called jacket, made of AISI 316LN in the DTT coils [11]. In Figure 1.3.2 the schematic representation of the cross-sections of the different DTT conductors is shown, with the gray part representing the steel jacket, the orange and red part is the cable (including also the space for the Helium circulation among the strands), and the blue circles are the holes, i.e. the pressure relief channels present only in the PF coils.
The TF cross-section of a dummy test conductor is then shown in Figure 1.3.3.

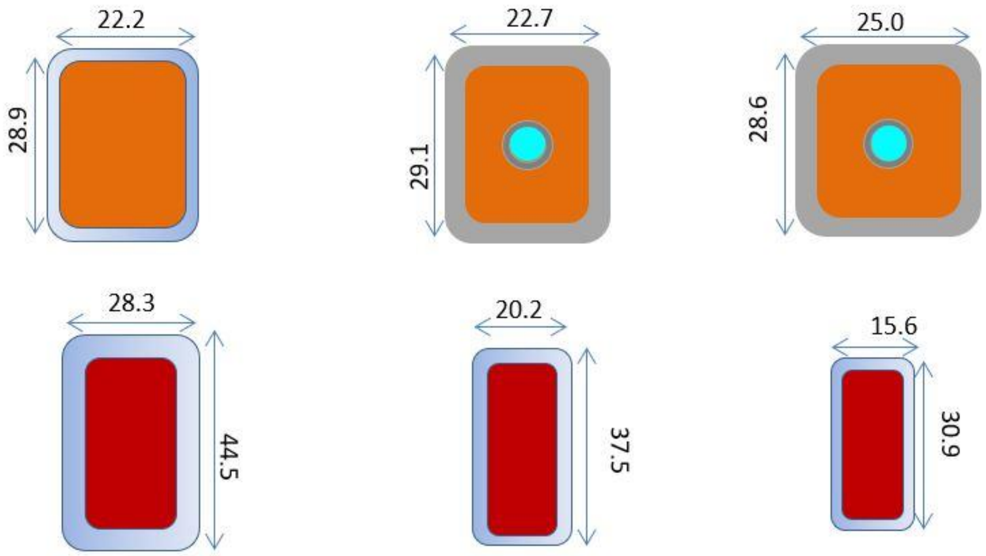

Figure 1.3.2: Cross section of the DTT conductors (dimensions in mm and at room temperature). From left to right and up to down: TF, PF1/6, PF2/5&PF3/4, CS high-, medium- and low-field [11].

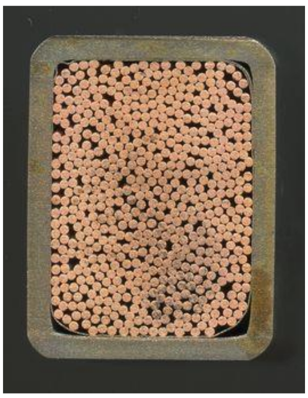

Figure 1.3.3: DTT-Test1-TF cross-section. Dummy Cu conductor tested by ICAS [12].

1.4 The SULTAN Facility

SULTAN (SUpraLeiter TestANlage) is one of the largest worldwide test facility for high current forced flow superconductors for fusion magnets (Figure 1.4.1). It is operated by EPFL-SPC (Swiss Plasma Center) and located at Paul Scherrer Institute (PSI) in Villigen, Switzerland. In the facility, prototype and R&D conductor samples can be tested over a wide range of operating conditions and magnetic fields up to 11 T. The main magnetic field is generated by three concentric pairs of superconducting split coils located inside a vacuum vessel and cooled by forced flow supercritical helium. The facility has two types of access for the sample: a vertical one for sample cross-sections smaller than 92 mm x 142 mm (bore dimensions) and a horizontal one for bigger samples, up to a diameter of 580 mm [13] (Figure 1.4.2). The vertical test well has at disposal a vacuum vessel separated from the one of the coils. This allows the insertion and extraction of samples in and out of the test well without having to break the vacuum and warm up the vessel of the SULTAN magnets. Therefore, the cool-down of a sample inserted in the vertical test well requires just a couple of days to reach 4.5 K.

A typical sample inserted in the vertical test well of SULTAN has two “legs” (called “left leg” and “right leg"), each containing either a conductor or a joint between conductors. The two legs are electrically connected each other through a bottom joint in praying hands layout.

In the vertical access configuration, the high current is provided by a superconducting transformer made of NbTi, whose primary winding can reach current values up to 200 A, whereas the secondary up to 100 kA [13]. The secondary winding is the one in electrical contact with the sample.

The temperature of the sample can be in the range 4.5-50 K. The upper extreme is of interest for the test of HTS conductors. If one wants to reach a temperature higher than 10 K, the sample is equipped with a HTS adapter for the electrical connection with the transformer and with a counter-current heat-exchanger, so that the heat flow to the LTS transformer is limited.

The maximum mass flow rate in one sample leg is 10 g/s, while the maximum pressure is 10 bar. The helium mass flow rate and temperature can be regulated separately in each of the two legs by means of two independent control valves and two independent heat exchangers.

Figure 1.4.1: The SULTAN Test Facility [13].

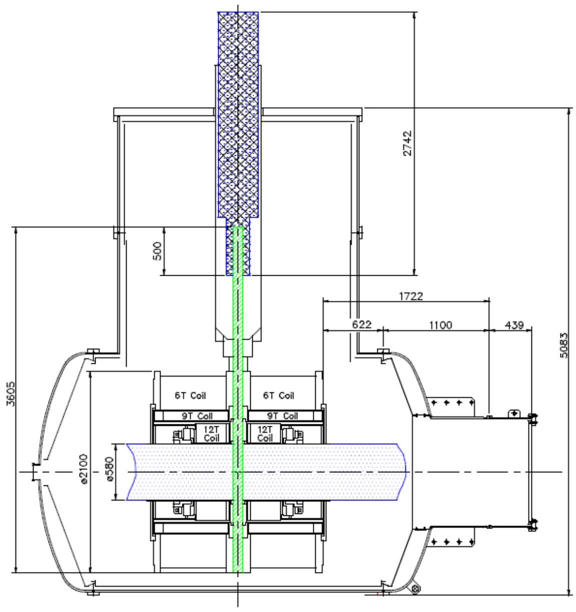

Figure 1.4.2: Sectional elevation of SULTAN. In green, the region for short conductor samples [13].

In AC loss measurements, the AC field is provided by a set of two copper saddle coils (Figure 1.4.3). The saddle coils can also be fed by a bipolar pulse battery for transient stability tests (quench tests). Through the discharge of such battery, a field rate up to 60 T/s can be reached with a discharge time of 128 ms. The pulsed coils are cooled indirectly with supercritical helium. To ensure that the coils are not overheating, a maximum power and pulse duration must not be exceeded. The maximum duration of the pulsed field depends on the field amplitude and on the DC magnetic field, which affects the resistance and hence the dissipated power of the copper winding [13].

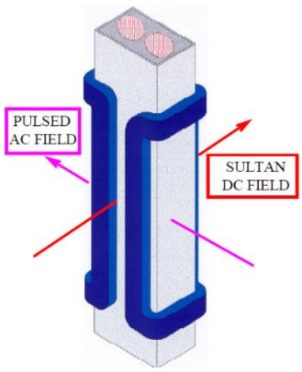

Figure 1.4.3: Sketch of the pulsed coils [13].

2. DTT TF cable specifications and preparation in SULTAN

2.1 TF cable samples specifications

The DTT magnet system will be built with superconducting cable in conduit conductors cooled by forced flow Supercritical Helium at 4.5 K. The Toroidal Field coils will use CICCs, with cables composed of twisted multifilament Nb_3Sn and chromium coated copper strands [11]. The high performance Nb_3Sn wire is being produced by Kiswire Advanced Technology Co, Ltd. (KAT). The wire design is based on the 0.82 mm strand supplied to ITER but with higher performances for critical current and AC loss [14]. The manufacturing process adopted by KAT for the Nb_3Sn wires of the DTT TF strands is the well-established *internal tin process* (information can be found in [15]), improved relative to the ITER strands by decreasing the copper fraction of the matrix area.

Two TF cable samples, representative of the final design geometry, were manufactured with the target processes and then tested in SULTAN to evaluate their performance. The design parameters of the two samples (TF-A and TF-B) are reported in the following Table 2. The differences between the two samples are in the cable twist pitch, shorter in the TF-B, and in the void fractions, slightly higher in the TF-B. The actual design difference between the two is in the twist pitch. For the final design and manufacture of the DTT TF coils there is the question of the cable performance with a certain cable twist pitch length and sequence. From previous analysis and computational simulations, it is known that cables with short twist pitch manifest smaller degradation caused by the electromagnetic force than cables with longer twist pitch, but higher AC losses than the others, particularly due to higher coupling currents [16]. Thus, the question on the final choice of twist pitch for the DTT TF coils must be solved by testing both the designs in SULTAN.

	TF- A sample (left leg)	TF-B sample (right leg)
Cable Pattern	[(1 Cu+2 Nb_3Sn) x 2 + 3 Nb_3Sn] x 3 x (4+Core) x 5 Core: 3 Cu x 4	
Number of Nb3Sn strands	420	
Number of Cu strands	180	
Cable twist pitch sequence (mm) (toll: +/- 5 mm on the first pitch; +/- 10 mm on the others)	100/110/125/140/300	82/135/180/220/290
Unit length (m)	10	
Cable direction	Right hand	
Target cable diameter (mm)	26.2	
Jacket thickness (mm)	1.9	
External dimensions (mm)	22.2x28.9	
cos θ (theta)	0.972	
Void fraction	27.6	27.7

Table 2: TF sample, conductor characteristics.

2.2 TF cable samples preparation in SULTAN

The two TF conductor samples have been manufactured by ENEA and sent to EPFL-SPC Superconductivity Group at PSI, Villigen by the end of April 2022. Upon arrival at SPC, the conductors are inspected for transport damages, the length and diameter are measured, and the conductors are marked with electric pencil for identification. Before testing in SULTAN, the sample must be prepared and instrumented. The conductor ends are dismantled for the assembly of the termination, which provide the electrical connections to the sample joint at the bottom end and to the SULTAN transformer at the upper end [17]. The cable pitch is estimated at the unwrapped cable and the cable surface is visually inspected for strand damage (Figure 2.2.1).

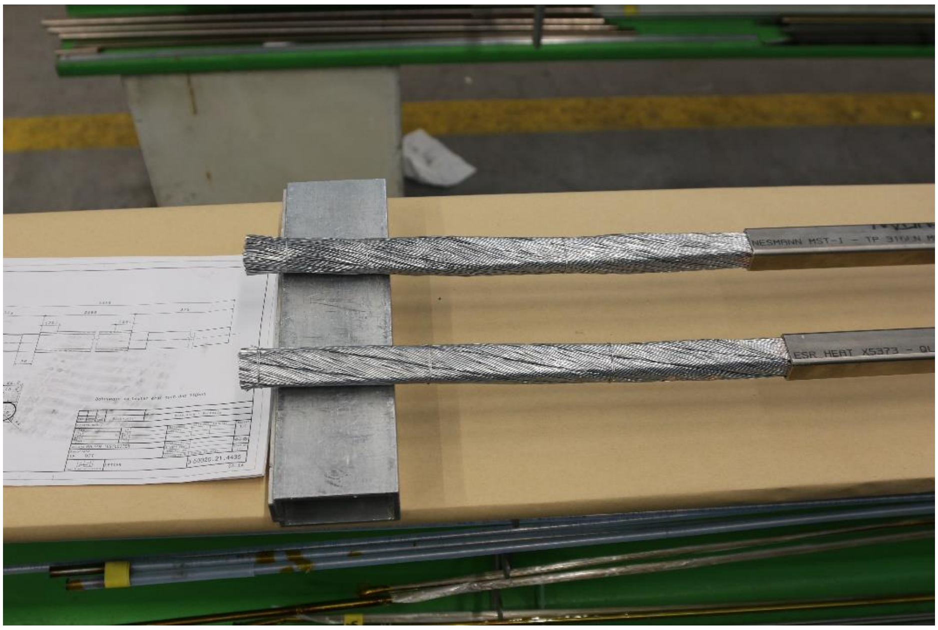

Figure 2.2.1: Sample after the removal of the cable outer wrap at the terminations.

The cable ends are dipped into an ultrasound bath with an acid solution for the removal of chromium plating (Figure 2.2.2). Two crimping rings are applied onto the conductor at both ends to prevent any slippage between conduit and cable upon cool down from the heat treatment. The conductor terminations are done by compacting a prefabricated copper sleeve with electron beam (EB) welded steel caps onto the cable after removing the Cr plating (Figure 2.2.3) [17]. A vacuum leak test is carried out on the prefabricated copper/steel assembly after EB welding.

Figure 2.2.2: Lowering the sample inside the ultrasound bath for Cr plating removal.

Figure 2.2.3: Conductor terminations with compacted prefabricated copper sleeves.

Figure 2.2.4: Sample insertion inside the vacuum furnace for heat treatment.

Then, the conductors undergo heat treatment for the activation of the Nb_3Sn superconducting phase. The treatment is conducted in one of the two vacuum furnaces available at SPC (Figure 2.2.4). The vacuum inside the furnace ranges between $2 \cdot 10^{-5}$ mbar and $3 \cdot 10^{-6}$ mbar [17]. A purge gas (Argon grade 5) is used inside the CICC sections of the samples to remove any dust from previous conductor manufacturing process. The overall heat treatment requires a duration of three weeks. Then, the conductor termination is solder filled by immersion in an ultrasound bath with the soldering material. The final result for the two conductors is shown in Figure 2.2.5.

Figure 2.2.5: Terminations of the DTT TF conductor samples.

In this phase, the additional pressure sensors required by ENEA have been installed on the right leg for the pressure drop measurement, as shown in the figure below (Figure 2.2.6). Two small holes have been drilled on the conductor jacket, at an exact 2 m distance. In the instrumentation phase, two capillary tubes welded on these holes are connected to a differential pressure transducer, and its signal is acquired during all measurement runs.

Figure 2.2.6: Picture of the hole drilled in the conductor jacket of the right leg, to which capillary tubes for the differential pressure measurement are attached.

The two conductors are then assembled to form the SULTAN sample that will be vertically inserted in the facility for testing. A copper plate is soldered to the upper termination of each conductor section to build the flat contact surface to the transformer in SULTAN (Figure 2.2.7). The termination plates are recovered after completing the test of the sample and recycled for other sample assembly [17].

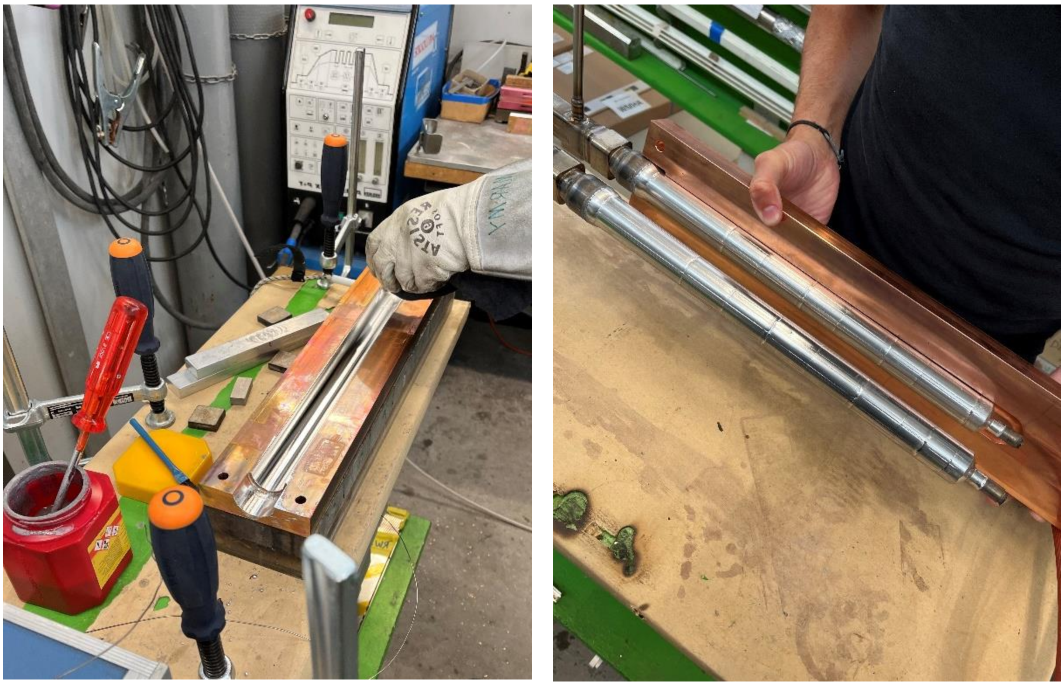

Figure 2.2.7: Copper plates for the upper termination. Application of Sn layer on the contact surface for soldering with SnPb eutectic alloy (left). Positioning of the copper plate on the termination (right).

After soldering the contact plates, sensors are installed in the two conductors. Two rings of voltage taps are applied on each leg by spot welding four stainless steel wires to the conduit, each rotated by 90°. Two sets of four CERNOX temperature sensors [17] are attached at two locations on each leg, upstream and downstream the center of the field generated by the SULTAN coils (Figure 2.2.8 c). The locations on the conduit where the temperature sensors are attached are machined flat. The attached sensors use bronze leads to limit the heat conduction to the sensor, and aluminum tape to provide a good heat sink to the conduit. This sensor attachment procedure is essential to obtain reproducible temperature measurements [17].

After the sensor installation, it is possible to complete the assembly of the SULTAN sample by inserting and soldering the lower joint to both lower terminations of the conductors, with the same procedure used for the upper terminations (Figure 2.2.8 a). Cooling is fundamental during soldering to not damage the installed sensors. After completing the soldering, a steel clamp is applied without insulation to the soldered joint.

The two conductors in the sample must be clamped together to withstand the strong electromagnetic repulsive loads in operation (Figure 2.2.9). A glass epoxy saddle is fitted between the two conductors and steel clamps are bolted together (Figure 2.2.8 b). Various slots are machined in the clamps at the locations of the voltage taps and temperature sensors, to allow the passage of the instrumentation cables (Figure 2.2.8 c).

a)

b)

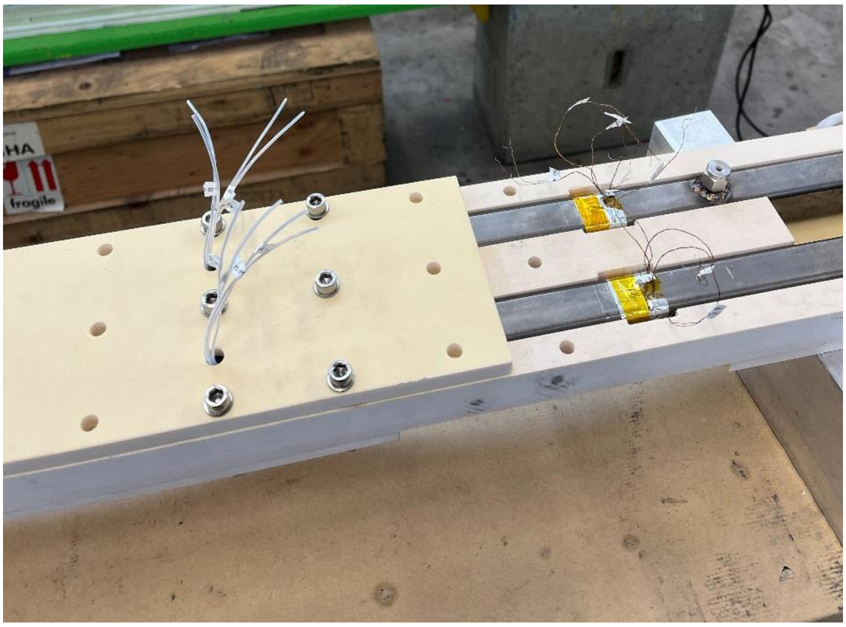

c)

Figure 2.2.8: Instrumentation and final assembly phase of the DTT TF SULTAN sample. a) View of the bottom joint with glass-epoxy insulating shell on the sides. b) Glass-epoxy plate covering the upper termination. c) Top glass-epoxy plate with holes for the instrumentation wires: Teflon covered wires from the voltage taps, yellow taped-wires from the CERNOX temperature sensors.

Figure 2.2.9: SULTAN sample after final assembly: the bolted steel clamps are visible on the sides (left). Zoom of the sample bottom region: the two gray tubes are for the Helium feeding to the two legs, the hole in the right is for the pressure capillary on the right leg, the green contact plates are for temperature sensors, which are wired and connected to the black wiring cable (right).

After assembly, the instrumentation is wired to the corresponded wiring cables with attached multi-pin connectors for the data acquisition system (Figure 2.2.9). The signals are then checked according to the standard procedure.

To fit in the SULTAN test well (144×94 mm) with a gap of 1 mm, four glass epoxy panels acting as "corner profiles" are bolted to the steel clamps. With these panels, the target cross-section of 142×92 mm is achieved [17].

The corner profiles guide the sample during the lowering into the SULTAN test well. A snapshot of the procedure is shown in Figure 2.2.10.

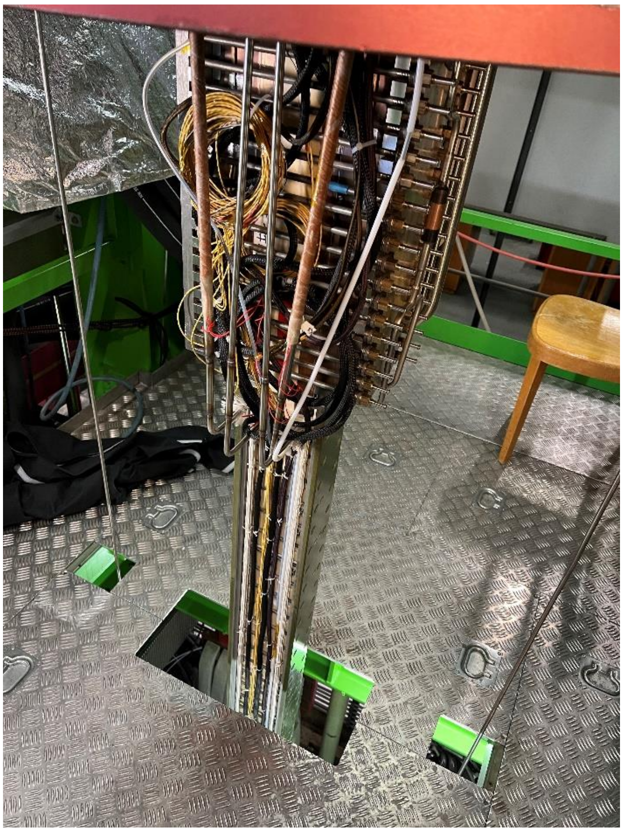

Figure 2.2.10: Lowering of the sample inside the SULTAN facility. Sample lifted with the crane above the lid valve, the telescopic cylinder needs to be lowered to open the valve (left). View of the upper termination of the sample, connection with the transformer and piping connection to the cryoplant (right).

At the end of the sample preparation, the two inlet and two outlet pipes are welded in their specific locations along the conductors. When the sample is installed in SULTAN, the pipes are connected with the cryogenic circuit of the facility (Figure 2.2.10), and the instrumentation cables are connected with the terminals placed in the top flanged head of the plant (Figure 2.2.11). From these terminations, the connection with the data acquisition system, placed outside of the facility, is achieved.

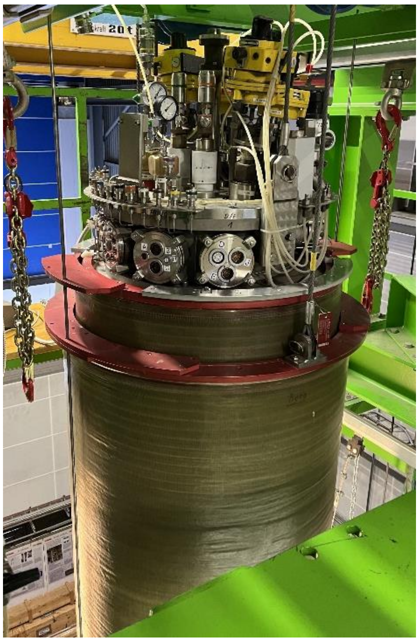

Figure 2.2.11: Top flange head of SULTAN, with valve-heads (yellow) and connector (on the top and sides) for the link of sample and plant instrumentation with the data acquisition system and control system. Below the flange, the telescopic cylinder (red and gray) used for the sample installation.

2.3 TF sample instrumentation

The DTT TF samples are equipped with the standard instrumentation scheme of an ITER TF SULTAN sample [17], and with the additional pressure transducer connected with capillary tubes in the right leg of the sample, for the precise pressure-drop measurement on a 2 m distance. The instrumentation scheme is shown in Figure 2.3.1, and the list of sensors in the sample is here reported:

- T1, T2, T3, T4 temperature sensors (four sensors each), placed at ± 400 mm from the field center of the two legs.
- T0L (320K), T0R (320K) temperature sensors placed at the helium inlet.
- VH1, VH2, VH3, VH4 voltage taps (four sensors each) placed at ± 225 mm from the field center of the two legs.
- V1/V2 voltage pair to sense the joint voltage drop.
- V3, V4 voltage taps next to the upper termination, connected with T-, T+ taps at the transformer plates, to sense V-drop over upper connections.
- PI absolute pressure transducer, and PI/PI pressure transducer for pressure drop measurement on the right leg.

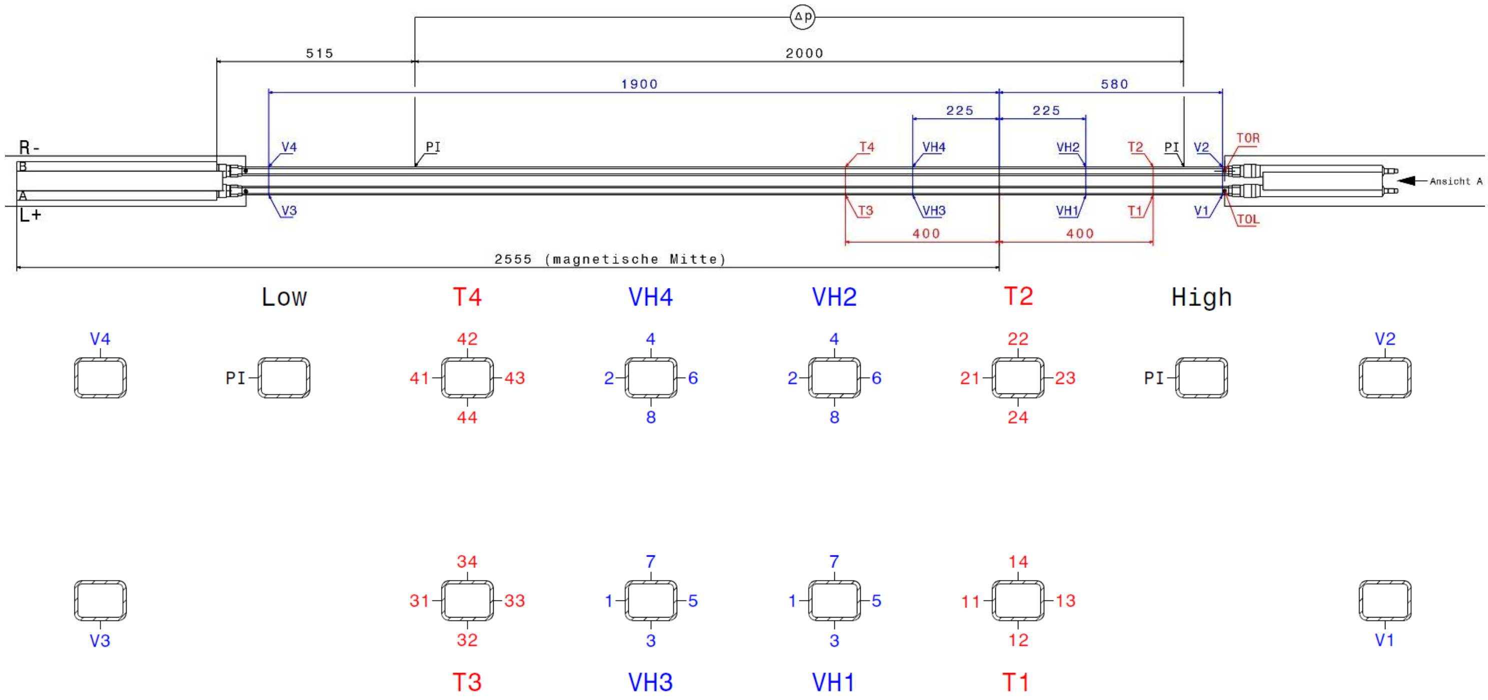

Figure 2.3.1: Instrumentation scheme for the DTT TF SULTAN sample (top figure). Schematic view of the sensor positions around the conduit section (bottom).

Besides the instrumentation mounted in the sample, the SULTAN facility can rely on mass flow meters downstream of the sample, pressure taps and temperature sensors on the inlet and outlet lines to the sample, heaters on the inlet feeding line for a dynamic regulation of temperature in both legs, and control valves on the outlet lines to regulate the He mass flow rate. Using the common nomenclature at SULTAN, the feeding lines includes the following:

- FI-953 (*dm/dt R*), FI-954 (*dm/dt L*) mass flow meters on the outlet lines of right (R) and left (L) legs
- PI-951/PI-953 (*P out R*), PI-952/PI-954 (*P out L*) pressure taps on the bench, pressure drop readings at about 15 m away from the sample
- TI-951G (*T in R 320K*), TI-952G (*T in L 320K*) temperature sensors on the inlet lines
- TX953 320K, TX954 320K temperature sensors on the outlet lines
- R951, R952 electric heaters mounted on the inlet feeding lines
- CV 970, CV 980 control valves mounted on the outlet sample lines .

The above-mentioned facility instrumentation is shown in Figure 2.3.2 with the simplified nomenclature used in any SULTAN data acquisition file during measurements. In the scheme the particular of the upper termination with the numenclature for the two conductor samples is also shown. The two ENEA conductors are identified from design as TF-A and TF-B samples. Inside the SULTAN sample they are commonly called legs, and in the following of this work it will be referred to the TF-A as *left leg* and to the TF-B as *right leg.*

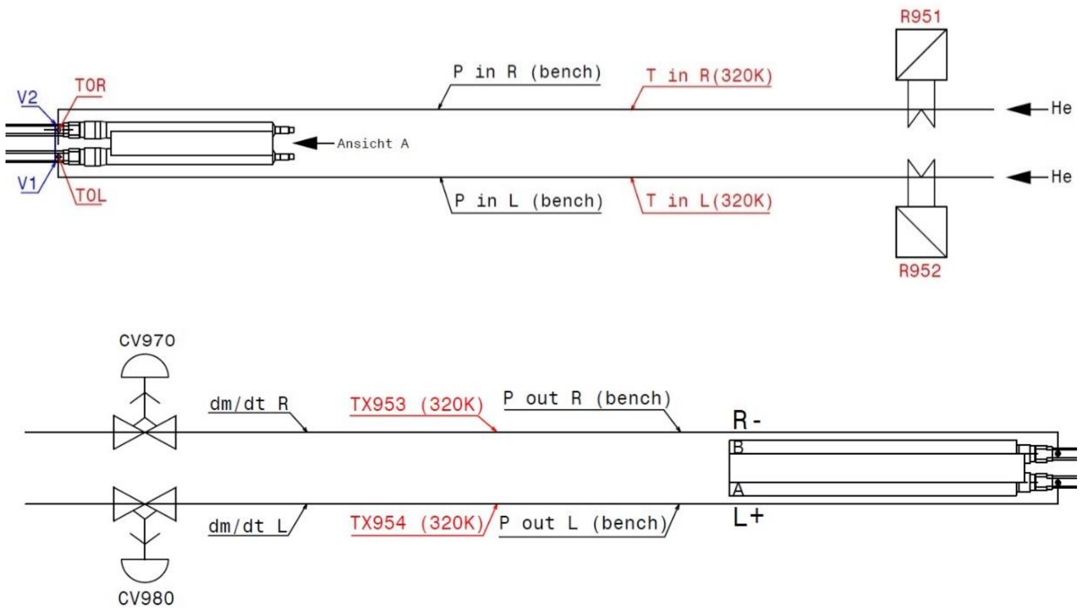

Figure 2.3.2: Instrumentation scheme in the inlet (top) and outlet (bottom) feeding lines to the SULTAN sample.

Besides the instrumentation on the Helium lines, in SULTAN the instrumentation for the electrical parameters is also present. The current and the voltage in the sample is recorded, as well as in the transformer, in the heaters and in the pulsed inductive coil for AC measurements. Also, the SULTAN magnetic field in the high field region is measured during experiments.

3. Tests of the TF samples in SULTAN

3.1 The testing program

The experimental campaign was assigned by ENEA to the EPFL-SPC Superconductivity group for the testing of the DTT TF conductor samples (TF-A and TF-B). According to the contract for the testing of the DTT coil samples [18], the reference operating conditions and the testing program used in the ITER or JT-60SA qualification campaigns [19], [20] have been taken as guidelines in the elaboration of the test requirements, and sometimes re-adapted to the specific conditions of DTT.

In the test requirement, the DTT TF coils main operative conditions are provided, ensuring that at SULTAN the samples are tested at conditions as close as possible to the operative ones.

The operative conditions are reported in the following Table 3.

Operative current (steady state)	42.5 kA
He inlet temperature	4.5 K
He inlet pressure	5 bars
He pressure drop (estimated)	2 bars
He mass flow rate (estimated)	4 g/s
Magnetic Field (peak)	11.8 T

Table 3: DTT TF coil main operative conditions.

The test program is redacted according to the objectives of ENEA for this conductor sample. The first goal is to measure the current sharing temperature (T_{cs}), for the definition of the minimum temperature margin of the coil, when subject to the background magnetic field in steady state [18]. Considering that during testing the two samples will generate a self-field, the SULTAN background field is chosen such that the resulting effective magnetic field value gives the target electromagnetic conditions for the CICC in operation.

Besides T_{cs} measurements, also tests for the pressure drop characterization in the TF-B (*right leg*) must be carried out. In these tests, values of pressure drop at different mass flow rate values, controlled by changing the outlet pressures (in steps of 1 bar starting from the lowest value up to 6 bar [18]), must be measured.

The AC loss characterization must be done up to 2 Hz to find the nτ parameter of the conductor and estimate the heat deposition during transient plasma scenarios. The conductor degradation must be analyzed with the application of up to 3000 electromagnetic cyclic loads, and with two thermal cycles of warm-up and cool-down (WUCD) of the conductor samples. The current sharing temperature is measured after 50-100-200-500-1000-1500-2000-2500-3000 cycles and after the two WUCD at 200 cycles and 3000 cycles. Critical current measurements must be done for the I_c and n-value measurement at the nominal magnetic field and at a temperature equal to T_{cs}+0.4 K. Measurements of current sharing temperature at different electromagnetic loads (different sample current and background field values) are fundamental to reconstruct the operation space of the conductor and analyze the effective strain behavior at different EM loads. In the end, the conductor stability must be tested with transient electromagnetic pulses, the tests of Minimum Quench Energy (MQE). With these tests is possible to obtain the minimum energy necessary to "quench" the conductor, so to make it transit from the superconducting state to the normal conducting state. The MQE tests are carried out at the operating electromagnetic conditions and different temperatures.

All these tests for the DTT TF conductor samples are practically collected in the *test program log file*, used in SULTAN to keep trace of the tests and the main outcomes during the experimental test campaign. A list of the test program used for the TF samples is reported here:

- Right leg (TF-B) pressure drop measurement at 4.5 K. Steps of mass flow rate of 1 g/s up to the maximum value (100% valve opening)
- AC loss measurements before DC tests (at begin of cycles, BoC). SULTAN field at 2 T, inlet temperature of 4.5 K, pulsed field of ± 0.3 T, pulse frequency in the range 0.1 Hz – 2 Hz, mass flow rate of 5 g/s and 2.5 g/s in the low pulse frequency tests

- DC Tests: T_{cs} measurement at nominal field and current (10.85 T and 42.5 kA). Current steps up to the nominal value, heating in temperature steps from the initial temperature of 4.5 K. Mass flow rate of 2.5 g/s.
- DC Tests: I_c measurement at BoC: test at T_{cs} + 0.4 K, current ramp with stop at 10 kA, mass flow rate of 4 g/s.
- DC Tests: T_{cs} measurement after cyclic load application (EM load of 10.85 T and 45 kA). Measurements after 50 – 100 – 200 cycles.
- DC Tests: I_c measurement after 200 cycles.
- AC loss measurement after cycling (before WUCD).
- *Warm-Up and Cool-Down (WUCD) of the sample*
- DC Tests: T_{cs} and I_c measurements after WUCD at 200 cycles.
- DC Tests: T_{cs} measurements after cyclic load application (10.85 T and 45 kA). Measurements after 500 – 1000 – 1500 – 2000 – 2500 – 3000
- DC Tests: I_c measurement after 3000 cycles.
- *Warm-Up and Cool-Down (WUCD) of the sample*
- DC Tests: T_{cs} and I_c measurement after WUCD at 3000 cycles.
- DC Tests: T_{cs} measurements at different loads: 10.85 T × 35 kA, 10 T × 42.5 kA, 10 T × 35 kA, 9 T × 42.5 kA, 9 T × 35 kA. I_c measured at 10 T.
- MQE Tests: Calibration Run at 9 T, zero current in the sample, inlet temperature of T_{cs} – 0.1 K for both legs, mass flow rate on each leg of 2.5 g/s. Runs with nominal current at different temperatures.
- AC loss measurements after cycling and two WUCD.
- Right leg (TF-B) pressure drop measurement at the end of the test campaign.

In the next sections, the test procedure and method of the reported test categories are explained.

3.2 Pressure drop characterization tests on TF-B

The prediction of the pressure drop to be expected in the DTT TF coils is of primary importance in the design of the cryoplant. The dimensioning of important systems, such as the supercritical He circulators, requires the measurement of the pressure drop on the straight conductor sample, and the rescaling and extrapolation of the pressure drop per unit length to the entire TF coil. The pressure drop characterization has been conducted only in the TF-B sample (the *right leg*), equipped with pressure capillaries installed by drilling two small holes on the conductor jacket at a 2 m distance. The two capillary tubes are connected to a differential pressure transducer, and its signal is acquired during each run by the Data Acquisition System.

The pressure drop characterization tests have been carried out at the beginning of the test campaign, before any electromagnetic loading ("virgin conductor"), and at the end, after electromagnetic load cycles and two thermal cycles of warm-up and cool-down of the sample. After electromagnetic and thermal cycles, strand movements and deformations due to Lorentz forces and thermal dilatation and contractions can change the hydraulic resistance of the supercritical Helium flow inside the CICC [21]. This can result in differences in the measured values of pressure drop at different values of mass flow rate. Thus, there is the need to test also after EM cycles and WUCD.

In these measurements, the conductor has been tested at zero SULTAN field and current, at a constant inlet temperature of 4.5 K. The mass flow rate has been varied in steps by manipulation of the outlet valve opening (CV-970 for the right leg), from a mass flow rate close to 0 g/s to the value corresponding to the full (100%) opening of the valve. In Figure 3.2.1 it is shown the time evolution of the mass flow rate and pressure difference at the capillaries for the two pressure drop characterization tests, namely the virgin conductor and at the end of EM and thermal cycles.

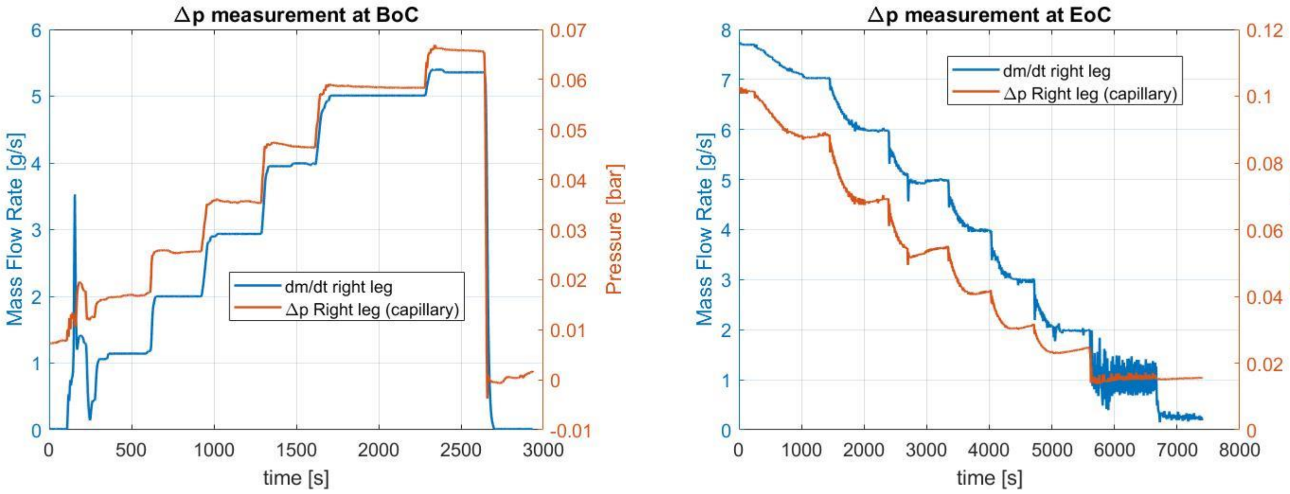

Figure 3.2.1: Time evolution of the mass flow rate and the pressure drop measured in the capillary. On the left, the test at the beginning of cycles, on the right the test at the end of the campaign

As it is visible from the comparison of the mass flow rate evolutions in the two pressure drop characterization tests, in the first test (at beginning of cycles, BoC), the maximum value of mass flow rate is around 5.4 g/s, corresponding to the maximum aperture of the control valve (CV-970). At the end of cycles (EoC), instead, it is registered a maximum value of 7.8 g/s. The reason behind this phenomenon is in the presence of an obstruction inside the TF-B conductor. It is still not clear the origin of the obstruction, whether it is the result of the soldering of some strands at the inlet, during the assembly of the lower termination, acting as a plug, or it is due to a not perfect vacuum inside the cable during the cool-down, with a cluster of frozen air in the region close to the inlet. The position of the obstacle is clearly in the inlet region, due to a pressure drop of about 7 bar with an inlet pressure of 10 bar, registered only by the pressure taps placed on the inlet and outlet feeding lines to the sample. The inlet pressure capillary is placed just after the inlet, from its measurement the pressure drop remains lower than 1 bar in the same experiment, and the recorded value of its absolute pressure is close to 4 bar. Thus, the obstruction is localized in the inlet region, upstream the first pressure capillary (Figure 3.2.2). Considering that with the 100% opening of the valve and an inlet pressure of 10 bar, it is expected a mass flow rate around 10 g/s, the presence of the obstruction reduces the mass flow rate of a factor two at BoC.

With electromagnetic load cycles and the two thermal cycles, the obstruction seems to be reduced (i.e., it has "cured"), so it shows a higher value of the maximum mass flow rate corresponding to the full opening of the valve. This can be a sign of the origin of the obstruction: if it is frozen air not removed inside the cable, the thermal cycles of WUCD have helped in partly removing the obstruction. But this does not exclude that it can be the fixation of some strands: the application of electromagnetic loads cause movements of the strands, which can separate and partly remove the plug. The final answer to the question of the origin of the obstruction will come from the destructive inspection of the cable sample, which will be conducted by ENEA in the next weeks.

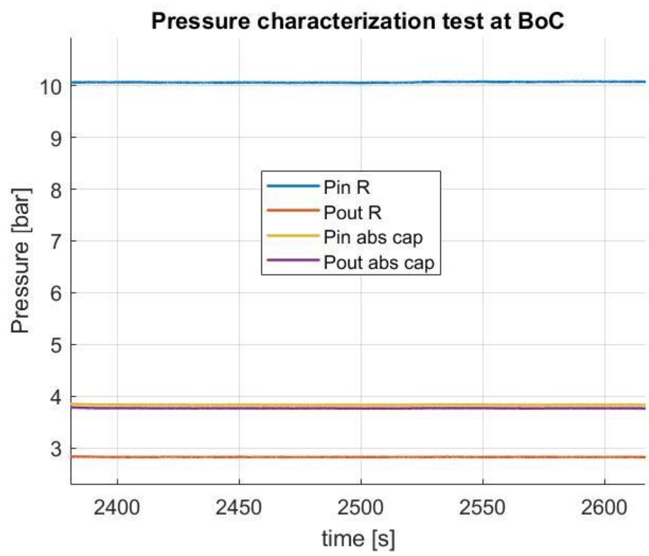

Figure 3.2.2: Zoom of the steady-state pressure evolution in the last plateau of the pressure drop characterization test at BoC. The 7 bar pressure drop with the bench pressure sensors, and the differences with the values from the capillary sensors are visible.

From the analysis of the temperature evolution during the hydraulic tests, another interesting behavior has been noticed particularly in the first pressure drop characterization run. In both the legs an unexpected temperature increase of about 0.25 K in the left-leg and about 0.5 K in the right leg has been experienced (Figure 3.2.3). Due to the very small static heat load present in these tests (no current in the sample, no Joule dissipation in the copper joint and termination), the enthalpy can be considered constant. The pressure, particularly in the right leg due to the presence of the obstruction, reduces to about 3 bar due to a 7 bar pressure drop, when the inlet pressure is kept at 10 bar.

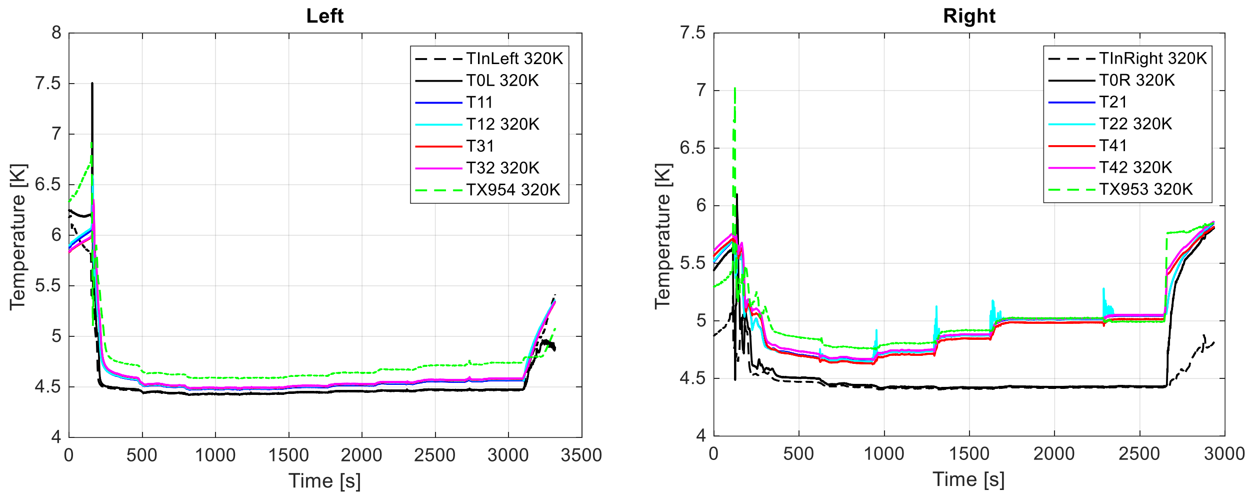

Figure 3.2.3: Temperature time evolution in the left and right leg for the pressure drop characterization test at BoC. Pressure range in the left leg: 10÷8 bar, in the right leg: 10÷3 bar.

In these conditions, the supercritical helium gas undergoes an almost isenthalpic lamination, from 10 bar to 3 bar in the right leg. For supercritical helium, the inversion point of the Joule-Thomson coefficient is around 50 K. Thus, at the testing temperature of about 5 K, to a pressure decrease it should not be associated any increase of temperature. This suggested that the possible cause of the helium heating during pressure drop characterization tests must be imputed to nonlinearities in the Helium properties. By the analysis of the He enthalpy behavior within the considered pressure range and temperatures, it resulted that in these conditions an isenthalpic transformation leads to a temperature increase (Figure 3.2.4). This has been also confirmed by a numerical simulation adopting the validated module of the 4C code for the cryogenic circuit analysis [22].

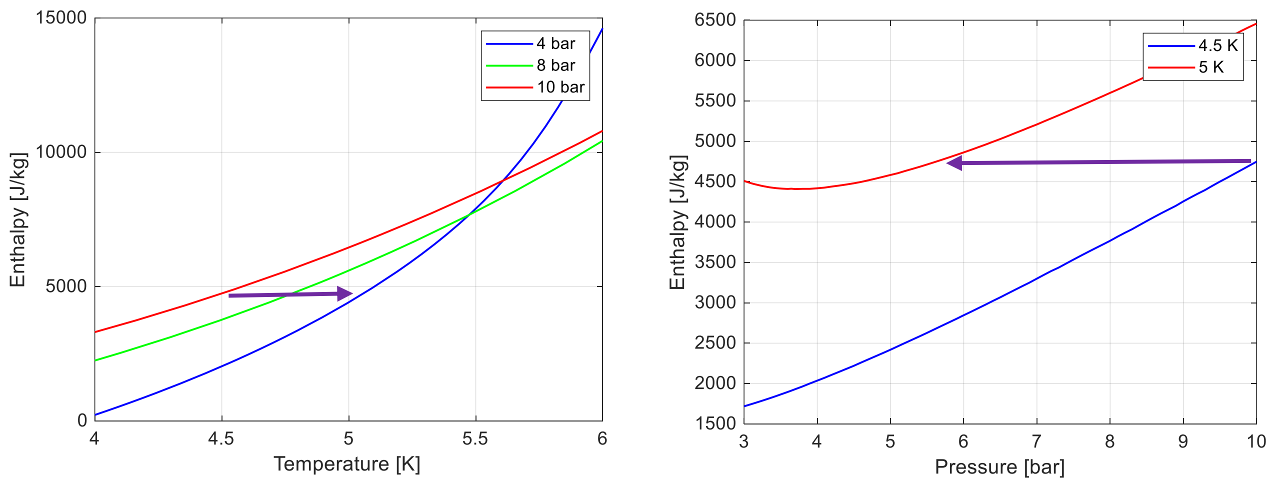

Figure 3.2.4: Enthalpy as a function of temperature (left) and pressure (right). Purple arrows show the temperature increase in an isenthalpic transformation at the considered range of pressure.

From the measurement of the pressure drop at different mass flow rates, it is possible to reconstruct the hydraulic characteristic of the CICC. To represent the values of pressure as a function of the mass flow rate, the recorded values are time-averaged in the intervals corresponding to the plateau ends. The averaging is fundamental to get a value representative of some hundreds of measurements, reducing the possible sensor fluctuations in the punctual values of a specific parameter. In this procedure, it is better to use the most stable interval of the plateau to avoid instabilities of the circuit. So, the interval at the end of the plateau is taken for the averaging of the mass flow rate and pressure.

It is also important in this procedure to remove as an offset the recorded value of pressure drop at zero mass flow rate. In the measurements in which it is not available, a parabolic extrapolation must be done on the measured data, to get the value of pressure drop at zero mass flow rate. The reading of this value from the capillary sensors results from the non-conservative hydrostatic contribution due to the unknown temperature distribution within the two capillaries, through their path from the conductor up to the sensor, that is installed at room temperature [21]. So, it must be removed from the measured values as an offset to get the actual value of the pressure drop due to the friction losses.

A further step in the pressure drop analysis is the derivation of the friction factor and of the Reynolds number from the measured data, to compare the results of *f(Re)* with the correlations for the friction factor available in literature for Cable-In-Conduit superconducting magnets for fusion applications. The friction factor is expressed with the Darcy's law, here reported:

$$\frac{\Delta p}{L} = 4f\frac{\dot{m}^2}{2\rho A_{He}^2 D_h} \tag{3.2.1}$$

With:

- f the Fanning friction factor, related by the equation $f_{Da} = 4 \cdot f$ to the Darcy friction factor.

- Δp the pressure drop.

- L the 2 m distance between the capillary pressure sensors.
- $\dot{m}$ the Helium mass flow rate in the conductor sample.
- ρ the Helium density.
- $D_h = 4A_{He}/P_w$ the hydraulic diameter.
- $P_w = (1 - k_{cj})P_{in,jk} + N_{strands}D_{strands}\pi k_c \frac{1}{2}\left(1 + \frac{1}{cos\theta}\right)$ the wetted perimeter [23]. The parameters k_{cj} (fraction of strands in contact with the jacket), k_c (fraction of strands in contact with He) are assumed equal to 0 and 5/6 respectively, $N_{strands}$ is the total number of strands, $D_{strands}$ the strand diameter, $cos\theta$ the twisting angle of the cable. $P_{in,jk}$ is the inner jacket perimeter.
- $A_{He} = A_{inner} - A_{strand}$ the Helium flow area. A_{inner} is the inner area of the jacket.
- $A_{strand} = N_{strands}\ \pi D_{strands}^2/4/cos\theta$ the total cross section occupied by the strands.

Defining the Reynolds number $Re = \frac{4\dot{m}}{\mu P_w}$ (with μ the dynamic viscosity) as a function of the measured mass flow rate, average capillary pressure and temperature from the mid temperature sensors (T4 from the instrumentation scheme), it is possible to represent the friction factor as a function of Re. The obtained values can then be compared with the results of some of the known hydraulic correlation for CICC for fusion magnets. The correlations used in this analysis are the Darcy-Forchheimer [24], the modified Darcy-Forchheimer [25], the Katheder correlation [26], and the JT-60SA correlation [27].

3.3 Current sharing temperature measurement tests

The current sharing temperature (T_{cs}) measurement is one of the main goals of the SULTAN experimental campaign for the first DTT TF conductor samples. As described in the introduction chapter, a superconducting material maintains its state under certain conditions of temperature, magnetic field and current. The critical temperature (T_c), the critical current density (J_c), and the critical induction field (B_c), define the limit conditions at which the superconducting state is manifested for a particular superconducting material. The parametrization of $J_c(B,T)$ identifies the boundaries of the *critical surface*. When the condition of the three parameters exceeds the boundaries, the current transport in the conductor is associated with resistive Joule heating.

When the cable operates at a temperature T_{op} below the critical current the material is superconducting. This state can be ideally maintained also at a temperature above the operative one, provided that the current is still smaller than the critical current. The current sharing temperature (T_{cs}) is defined as the temperature at which the critical current equals the conductor operating current [28]. Above T_{cs}, the superconductor develops a resistance, and the current flow is associated with dissipative Joule heating. In the normal conducting state, superconducting materials such as Nb_3Sn, manifests high electrical resistivity compared to normal conductors in cryogenic conditions. For this reason, in CICC cables for fusion applications, the superconducting filaments are immersed in a copper matrix, and a certain number of copper strands is placed in the cable. When T_{cs} is reached, the current flows preferably in the copper strands for their lower electrical resistance. This regime of current transition from the superconducting strands is commonly called *current sharing regime*. The copper inside the CICC is called *stabilizer* for its role in overtaking the current when the superconducting filaments transits to the normal conducting state, and it is fundamental in any technical application of superconducting cables.

During the transition to the normal conducting state, a resistive voltage (i.e., an electric field) starts developing in the conductor. The development of the resistive longitudinal electrical field in high current density superconductors is known to be exponential versus current, magnetic field or temperature, following with good approximation this equation [29]:

$$E = E_C \, exp\left(\frac{T - T_{cs}}{T_0} - \frac{I - I_c}{I_0} - \frac{B - B_{cs}}{B_0}\right) \quad (3.3.1)$$

With E_C the critical value of the electric field used as criterion for the definition of the critical current. This criterion definition is important for the inter-laboratory comparability of the measured data, considering that the electric field appearance starts before reaching the critical current [30]. The value of $10\ \mu V/m$ is commonly used in low temperature superconducting magnets for fusion applications. B_{cs} is the value of the magnetic field when T_{cs} is reached. The increments T_0, I_0 and B_0 are function of temperature, magnetic field and critical current, and are related to the broadness of the transition to the normal conducting state. In current sharing measurements the current and the magnetic field are maintained constant, to avoid any additional temperature rise in the regions in which inductive electric fields are generated due to variations of current and/or magnetic fields [31]. In these conditions equation (3.3.1) simplifies in:

$$E = E_C \, exp\left(\frac{T - T_{cs}}{T_0}\right) \quad (3.3.2)$$

In T_{cs} measurement analysis, rather than the expression reported above, a common empirical correlation for the temperature transitions is adopted [32]. The correlation follows a power-law structure, symmetric to the E-I transition scaling law (described in the Section 3.3), with the definition of the *m-index* to effectively describe the broadness of the transition. The equation is here reported:

$$E = E_C \left(\frac{T}{T_{cs}}\right)^m \quad (3.3.3)$$

The current sharing temperature measurements are fundamental in the stability analyses of the conductor. During the operation in a reactor, the superconducting magnets are subjected to heat perturbations and static loads coming from the plasma (neutron heat load), from inductive pulsed fields which can induce AC losses (even in the DC operated TF coils, from the flux generated in the central solenoid), from heat leaks through the magnet insulation, through the joints and terminations and through the instrumentation ports. Also, the strands movements and deformations when subjected to EM loads (Lorentz forces) result in heat dissipations by friction [28]. The criticality in the design of superconducting magnets is whether the heat deposition during operation can result in a transition to the normal state (i.e., overcoming the current sharing temperature). For this reason, it is important to address the conductor stability defining the *temperature margin*, which is the difference between the current sharing temperature and the operative one [28].

For the DTT TF coils, the design requirement for the minimum temperature margin is equal to 1.4 K [33]. Predictive numerical simulations [34] are used to estimate the stability of the conductor and of the whole magnet system during operation, and they come to support in some important design decisions. To this, a complementary and fundamental contribution comes from the experimental tests and analysis on the conductor samples.

In SULTAN, the T_{cs} tests for the DTT TF conductor samples were performed in normal operating conditions, with repeated measurements after the application of cyclic electromagnetic loads and two thermal cycles, to analyze the cable degradation. Also, tests with different EM loading conditions have been conducted, to reconstruct the operation space of the conductor and analyze the effective strain behavior at different EM loads. In the measurements at nominal conditions, to test the conductor with the operative field and current, it has been considered that during testing the two samples will generate a self-field. So, the SULTAN background field has been chosen such that the resulting *effective magnetic field* value gives the target electromagnetic conditions for the CICC in operation. The procedure used to compute the effective magnetic field is described in Appendix A.2.

In Table 4 the parameters for the T_{cs} measurements done in SULTAN are reported.

T_{cs} measurements	B SULTAN [T]	I sample [kA]	dI/dt [A/s]	T Left [K]	T Right [K]	dm/dt L [g/s]	dm/dt R [g/s]
EM and thermal cycles measurements after 0, 50, 100, 200, 200(WUCD), 500, 1000, 1500, 2000, 2500, 3000, 3000(WUCD) cycles	10.85	42.5	100	4.5	4.5	2.5	2.5
Measurements with different loads (after 3000 cycles and WUCD)	10.85	35					
	10	42.5					
	10	35					
	9	42.5					
	9	35					

Table 4: SULTAN parameters for the T_{cs} tests of the DTT TF conductor samples.

The testing procedure used at SULTAN for the measurement of the current sharing temperature consists in first ramping up the current step by step, up to the desired operating value. The steps are done at 0, 10, 20, 30 kA and the last step is at the target current of 42.5 kA or 35 kA depending on the test. Then, the temperature is ramped up, also step by step, with plateau sufficiently long for the temperature and electric field stabilization. The values of the electric field computed from the voltage measurements divided by the distance between the voltage taps ($E = \Delta V/\Delta L$, with $\Delta L = 450\ mm$, see Figure 3.3.1), are monitored together with the temperature in the high field zone (sensors T1, T2, T3, T4) and current evolution.

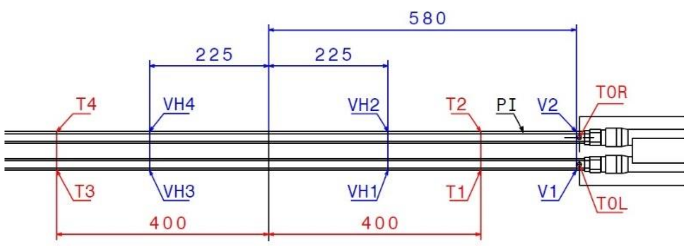

Figure 3.3.1: Zoom of the instrumentation scheme of the DTT TF SULTAN sample. The voltage taps considered in the analysis for the electric field computation are the VH2/VH4 and VH1/VH3, at a 450 mm distance.

In experimental tests is conventionally established the T_{cs} value as the temperature measured when the average electric field reaches the criterion of $10\ \mu V/m$ [35], as expressed in equation (3.3.3). If the two conductor legs show a significantly different current sharing temperature (as it is the case for the TF-A and TF-B samples), the operator employs a differential heating of the two legs (i.e., lower – faster heating rates for the two legs) to maintain the two electric fields as close as possible while crossing the $10\ \mu V/m$ criterion. This gives more stable and comparable results and avoids the normal state transition of one of the two samples before the other has reached the criterion for the T_{cs} measurement.

The evolution of the measured current in the sample, voltage and temperatures in the high-field zone for the two TF conductors during one of the T_{cs} tests at nominal operating conditions is shown in the following Figure 3.3.2. The data names are those used by SPC during the test campaign.

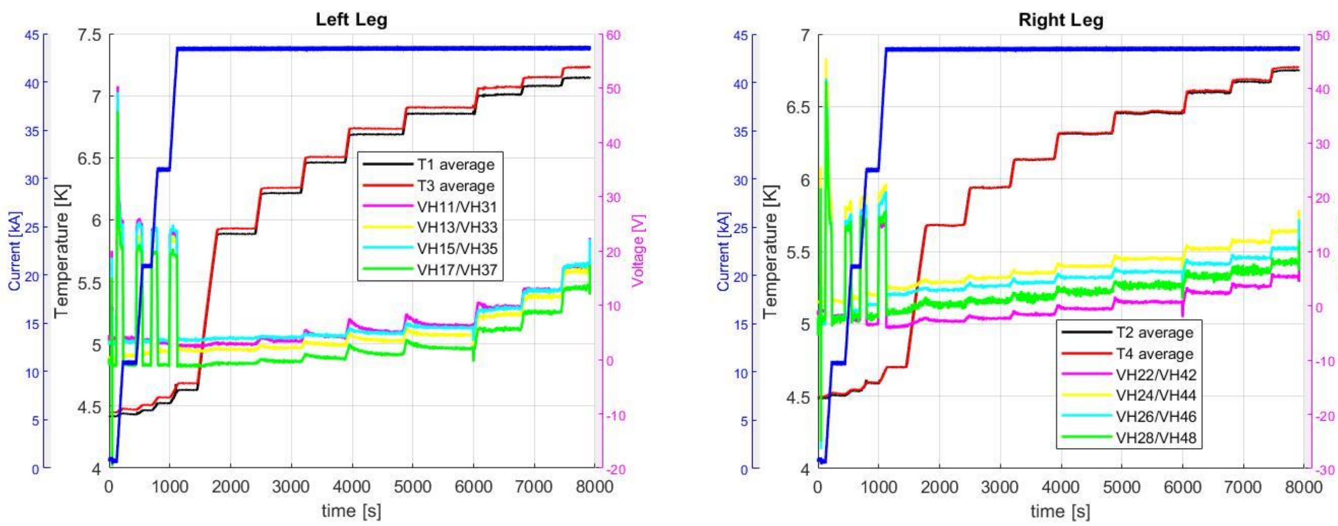

Figure 3.3.2: Time evolution of temperature, voltage and current for the T_{cs} test after 3000 cycles and WUCD.

For the experimental assessment of the T_{cs}, two methods are considered: the *voltmetric method* and the *calorimetric method*. The voltmetric method is the most common, considered the good precision of the voltage sensors measurements in the conductor samples, and the only adopted in this work. The calorimetric method is instead considered as a backup, used only in cases in which the voltage sensor readings are unreliable [35].

In SULTAN the analysis follows the standard testing requirements from the ITER data reduction procedure [35]. According to the ITER instructions, the voltage and calorimetric data reduction is based on the quasi-steady state values that are achieved at the end of each of the current and/or temperature steps, once relaxation is complete. Before implementing the T_{cs} analysis, an important step consists in checking the sensor response to track and possibly discard those sensors which are showing some inconsistency. *Calibration runs* are performed for that purpose at the beginning of the test campaign. In these tests, the level of the voltage offsets is checked, as well as their possible variation with temperature, and the possible inconsistencies in the temperature sensor readings.

The current steps are considered in the ITER analysis for the extrapolation of a *linear voltage offset*, to be subtracted to the measured voltage values to account for the inductive voltage contribution due to the ramping of the current. This procedure must be followed if the electric field value at the end of the current ramp overcomes $1\ \mu V/m$. In this work, the linear offset removal proposed in the ITER testing procedure has not been used. Instead, a constant voltage offset has been removed at the end of the current ramp, within the corresponding temperature step, after relaxation (Figure 3.3.3). The obtained results are complementary to the ITER data reduction once the current has reached the nominal target value.

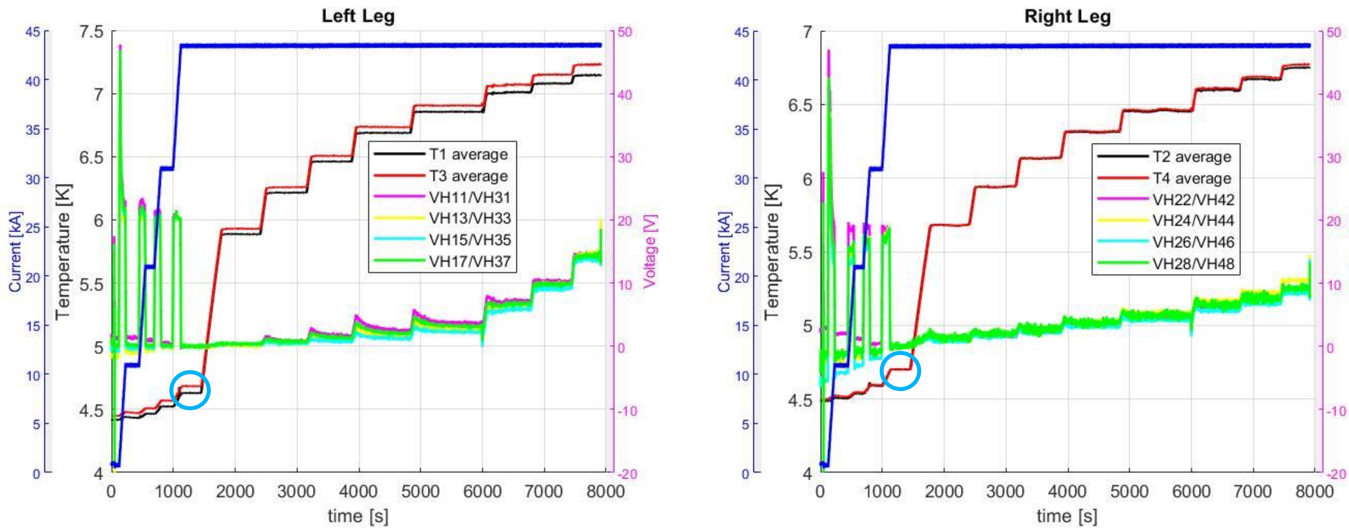

Figure 3.3.3: Evolution of current, voltage and temperature in the two sample legs after removing the inductive voltage offset in the shown temperature step after the current ramp (cyan circle). T_{cs} measurement test after 3000 cycles and WUCD.

After removing the inductive offset from the voltage measurements, the data reduction is followed. The voltage and temperature values in the steps are time-averaged in the intervals corresponding to the plateau ends, to get a value representative of some hundreds of measurements, reducing the possible sensor fluctuations due to voltage and cryogenic-circuit instabilities. The computed average voltage values for each sensor are divided by the length between the voltage taps and, together with the average temperature values, the E-T characteristics are represented. The average voltage from the four pairs of voltage taps in each leg is computed and taken as reference value for the E-T characteristics. In the representation, the $log_{10}(E)$ is taken and a horizontal line in correspondence to $10\ \mu V/m$ clearly shows the electric field at the criterion. To obtain the T_{cs} value from the measurement test, the E-T power law (Equation 3.3.3) is best-fitted to the points closer to the criterion. From the fit, the T_{cs} value and the m exponent for the broadness of the transition are obtained within a certain confidence bound from the interpolation.

In several measurements for the DTT TF conductor samples, a change of slope in the $log_{10}(E)\ vs\ T$ plot was experienced from the one or two points below the criterion, to the three or four above of it. For this, two different interpolations of the E-T power law have been used, and two different resulting values for the T_{cs} and m-index have been computed. From a critical analysis of the results (described in Section 4.2), it is evident that the more reliable values where those coming from the interpolation of the points across the criterion, so from the second slope present in the E-T characteristics. Thus, in the experiments in which this phenomenon appeared to be relevant, only the results from the power law fit across the criterion have been used in the stability and degradation analyses. Figure 3.3.4 shows the resulting plots for the E-T characteristics, with the vertical marks around the average electric field (i.e., average voltage values) for the field values computed from the single sensor couples (VH22/VH42, VH24/VH44, etc.). The two power law fits are represented with the green and blue dashed lines, being SLOPE#2 fit the one used in the analysis.

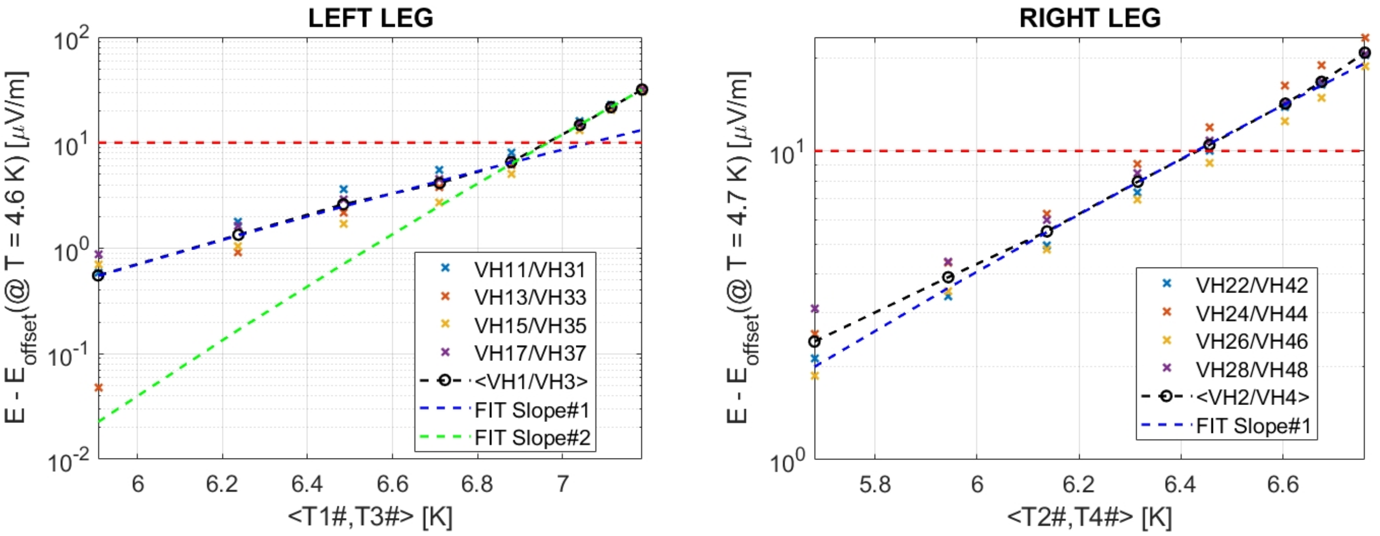

Figure 3.3.4: E-T characteristics for the T_{cs} measurement test after 3000 cycles and WUCD. Log scale used in the y-axis. The red dashed line marks the criterion, black dotted line for the field values from averaging of the voltage sensors. Results from single V-taps couples represented with "x" marks. Left leg affected with double-slope, second slope represented with green dashed line.

In formulas, the procedure for the analysis of the T_{cs} measurement tests follows the reported steps:

- Determination of the average constant voltage offset in the stabilized interval of the temperature plateau after reaching the nominal current:

$$\Delta V_{offset} = \frac{1}{N_{sample}(\Delta t_{offset})} \sum_{j=1}^{N_{sample}} \Delta V(t_j) \tag{3.3.4}$$

With $N_{sample}(\Delta t_{offset})$ the number of acquired voltage values in the considered interval. The denomination ΔV_{offset}, $\Delta V(t_j)$ is generic for the voltage sensors couples VH11/VH31, VH13/VH33, etc.

- Offset removal and division by the distance between the voltage taps to obtain the corresponding electric field value:

$$E(t) = [\Delta V(t) - \Delta V_{offset}]/\Delta L \tag{3.3.5}$$

- Averaging of the electric field and temperature values in the stable intervals of the plateau (*n* generic step):

$$E(\Delta t_n) = \frac{1}{N_{sample}(\Delta t_n)} \sum_{j=1}^{N_{sample}} E(t_j) \tag{3.3.6}$$

$$T(\Delta t_n) = \frac{1}{N_{sample}(\Delta t_n)} \sum_{j=1}^{N_{sample}} T(t_j) \tag{3.3.7}$$

With T, generically referring to the four-sensor average of the temperature sensors in the high field zone (HFZ): T1, T3 in the left leg, T2, T4 in the right leg.

- Then represent the E-T characteristics applying the logarithm: $log_{10}\big(E(\Delta t_n)\big)$, and interpolate the values closer to the criterion with the power law (equation 3.3.3), to determine the two free-parameters of the fit:

$$y = C\left(\frac{x}{a}\right)^b \tag{3.3.8}$$

Substituting C with the critical field value corresponding to the criterion and solving the equation for $x = T$, the T_{cs} value is determined from parameter a, and the m-index from the exponent b.

The procedure described for the analysis of the T_{cs} measurement tests has been carried out with MATLAB [36]. The power law interpolation was handled with the built-in function *fit,* which returned the confidence bounds together with the results of the T_{cs} and *m-value.*

3.4 Critical current measurement tests

In the SULTAN testing of the DTT TF conductor samples, in addition to the T_{cs} tests, measurements of critical current were requested at the begin of the test campaign (for the virgin conductor), before and after the EM load cycles and the two warm-up and cool-down thermal cycles. As defined in the previous section, the critical current I_c represents one of the boundaries of the *critical surface* for a superconducting material, and for this reason it is defined as the maximum current that a superconducting wire can carry remaining in the superconducting state [37]. The critical current measurement is fundamental in the characterization of superconducting wires, being a target parameter of the performances of the superconductor and essential in the parametrization of the critical surface of the superconducting wires (described in Appendix A.1). Measurement tests of I_c are fundamental also for the characterization of the performances of CICC cables. The resulting I_c values from the CICC testing are compared with the strand critical current to understand the effectiveness of the CICC and the utilization of the strand properties [31]. In the strand characterization tests, the critical current measurements are also used to assess the strand degradation through V-I characteristics, considered the low magnetic self-field contribution in single-strand measurements. In SULTAN tests, large CICC conductors can present evident inductive noise during V-I transitions, with changes in the effective magnetic field, current redistributions and temperature rises in the joints and due to self-heating in the area that generates electric field [31]. For this reason, T_{cs} measurement tests (i.e., V-T transitions) are preferred for the analyses of degradation. However, in the present work from the obtained results on the TF samples, an analysis of degradation is also presented for the I_c measurements conducted at the same testing temperature. In the previous section it was described that the normal-state transition for a superconducting cable presented an exponential growth of the longitudinal electric field over current, magnetic field and temperature (Equation 3.3.1).

Assuming constant temperature and magnetic field, it is common to represent the V-I characteristics, i.e. the resistive transition of the superconductor, using the purely empirical power law correlation [28] here reported:

$$E = E_c \left(\frac{I}{I_c}\right)^n \tag{3.4.1}$$

With E_c the critical value of the electric field used as criterion for the definition of the critical current. As reported in the previous section, it is common to fix the criterion at the value of $10\ \mu V/m$. The exponent n is a fundamental parameter for the technical application of superconducting cables, defining the *sharpness* of the transition to the normal conducting state. A low value of the exponent n corresponds to a milder and broader transition, while a high value of the exponent results in sudden transitions. This parameter has implications on the stability of the superconducting cable, being more or less resilient to thermal instabilities, ensuring or not the possibility to recover a normal transition without resulting in a thermal runaway (i.e., a *quench* phenomenon). On the other hand, lower values of exponent n corresponds to the appearance of a resistive voltage before reaching the critical current. With lower n we should expect a small current transferred to the copper stabilizer already below critical conditions, and this affects the performance of the cable. Thus, in practical superconducting magnet applications for fusion, for Nb_3Sn superconducting CICCs the n-*value* is usually targeted in the range of 5 – 15 [38].

In SULTAN, the critical current measurements for the DTT TF samples have been performed before the application of EM load cycles, before and after the two thermal cycles of warm-up and cool-down at 200 and 3000 EM load cycles, and at reduced SULTAN background field of 10 T after 3000 EM load cycles and WUCD. The conductors have been tested at a temperature of $T_{cs} + 0.4\ K$, to measure the critical current without overloading the conductor. When the temperature has reached this value slightly higher than T_{cs}, the current is started ramping continuously towards the nominal value. The parameters for the I_c measurement tests done in SULTAN for the DTT TF samples are reported in Table 5.

Ic measurements	B SULTAN [T]	I sample [kA]	dI/dt [A/s]	T Left [K]	T Right [K]	dm/dt L [g/s]	dm/dt R [g/s]
Before EM cycles	10.85	0-10-42.5	100	6.7+0.4	7.1+0.4	4	4
Before WUCD at 200 EM cycles				7+0.4	6.5+0.4		
After WUCD at 200 EM cycles				6.9+0.4	6.4+04		
Before WUCD at 3000 EM cycles							
After WUCD at 3000 EM cycles							
Measurement at 10 T after 3000 cycles and WUCD	10	0-10-55		7.6+0.4	7.1+0.4		

Table 5: SULTAN parameters for the I_c measurement tests of the DTT TF conductor samples.

The testing temperature for the I_c measurements derives from the T_{cs} tests, the differential heating of the two samples controlled by the two independent electrical heaters in the He feeding lines, gives the possibility to set the two measured T_{cs} on the respective sample legs. It must be noted that in the first I_c measurement (before EM cycles) due to a wrong temperature set-point in the resistive heaters, the two T_{cs} for the *left* and *right* leg have been inverted. This, as it will be pointed in the results chapter, lead to a failed measurement of the critical current in the *left-leg* (TF-A), because of the un-reached electric field criterion. In the other I_c measurements, the target temperature of $T_{cs} + 0.4\ K$ has been obtained from the T_{cs} measurement at 200 EM cycles for the I_c before WUCD (at 200 EM cycles), while for the other three measurements at nominal field the T_{cs} measured after WUCD at 200 cycles has been used. Repeating the tests after different EM thermal loads, maintaining the same testing temperature, enables the comparability of the results. For these measurements a degradation analysis has been done in the present work (Section 4.3).

In the last measurement at reduced field of 10 T, the T_{cs} temperature from the measurement at 10 T and 42.5 kA has been employed.

In SULTAN, the procedure for the critical current measurement tests consists in ramping up the current while maintaining the temperature of the samples at the values of $T_{cs} + 0.4\ K$. During the current ramp, a steady state interval is maintained at 10 kA for the current offset correction, due to possible unbalances in the current set-value in the SULTAN transformer. From this step at 10 kA, the current is then ramped up continuously to the nominal value. The I_c is obtained at the value of the electric field criterion before reaching the nominal current. In the SULTAN analyses of critical current, the temperature and voltage measurements in the high field zone (HFZ) are monitored together with the current in the sample. Figure 3.4.1 shows the evolution of these parameters during the I_c measurement after WUCD at 3000 EM cycles.

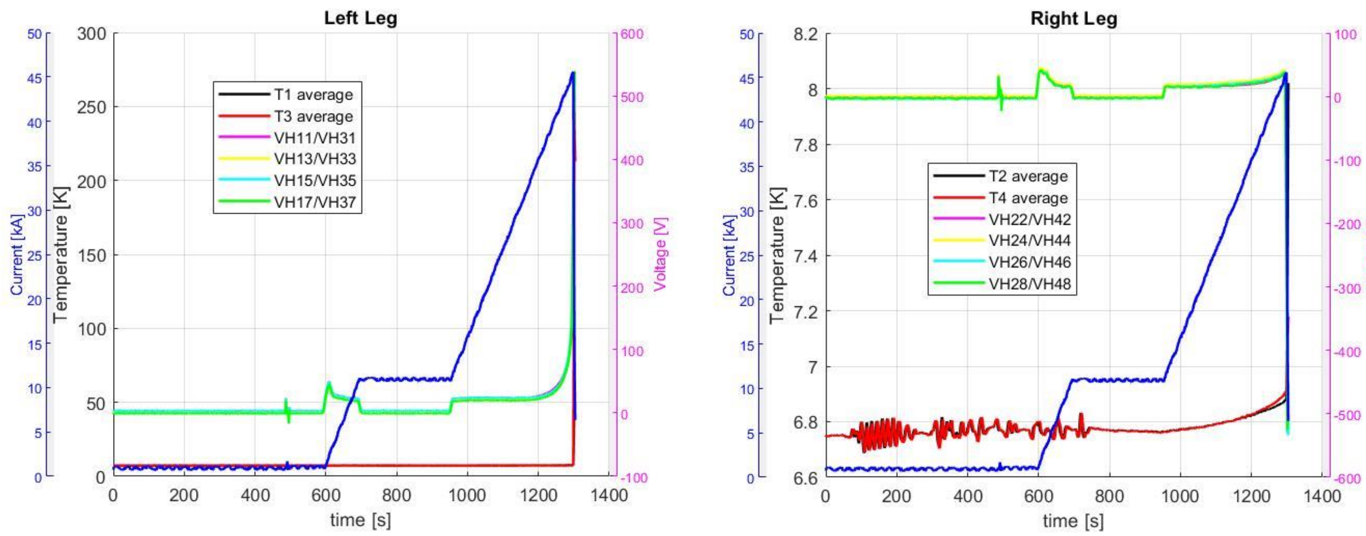

Figure 3.4.1: Evolution of the current in the sample and the voltage and temperature measurements in the HFZ for the two sample legs. Test after 3000 EM cycles and WUCD.

As seen in the T_{cs} measurements, also for the I_c the voltage and temperature sensors taken as reference in the analysis are those located in the SULTAN high field zone. In this spatial region, the SULTAN magnetic field generated from the coils has reached a uniform distribution, settling to the desired magnetic field level. In this region the voltage measurements are less affected from the magnetic field distribution, thus their values can be considered more reliable.

After the current step at 10 kA, a voltage offset needs to be removed to neglect the inductive voltage contribution developed during the current ramp. In a time interval after the current step, when the temperature is stable, the constant voltage offset is computed by averaging the voltage measured data within the selected interval, with the same procedure used in the T_{cs} measurement tests:

$$\Delta V_{offset} = \frac{1}{N_{sample}(\Delta t_{offset})} \sum_{j=1}^{N_{sample}} \Delta V(t_j) \tag{3.4.2}$$

The offset is then subtracted to the voltage values and the electric field is obtained dividing by the distance between the voltage sensors.

$$E(t) = [\Delta V(t) - \Delta V_{offset}]/\Delta L \tag{3.4.3}$$

Then, for the characterization of the V-I transitions all the $E(t)$ values have been represented in plots as a function of current. The $\log_{10}$ of $E(t)$ and I *sample* have been applied for the linearization of the V-I transitions, and the electric field values have been normalized to the criterion. The resulting V-I characteristics from the single voltage taps couples are reported in Figure 3.4.2, the criterion corresponds to the value of 10^0.

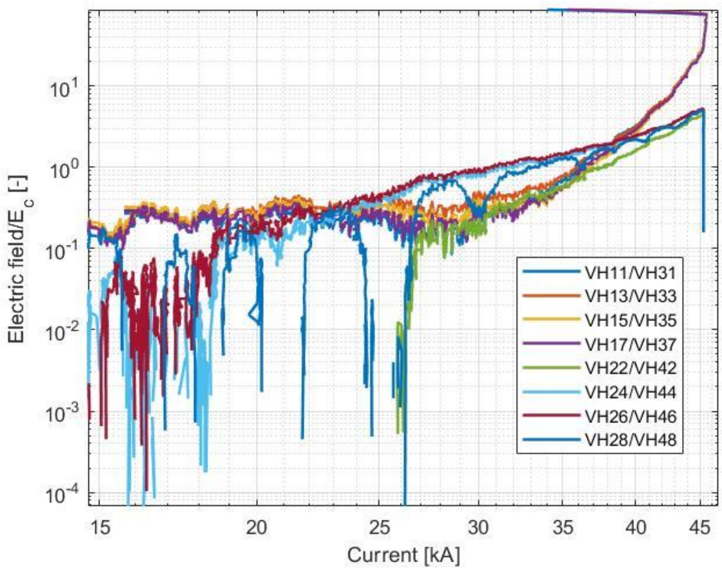

Figure 3.4.2: V-I characteristics for the I_c test after WUCD at 3000 EM cycles. Electric field values from the voltage taps pairs the two sample legs.

From this plot, a current range is selected for the analysis of the transition. The range avoids the electric field instabilities present at low currents, and discards the higher current values (close to the nominal current or slightly higher) at which the sudden thermal runaway (*quench event*) results in the activation of the SULTAN *quench protection system* for the current discharge, avoiding damages to the conductor samples and to the SULTAN transformer. In this range, the electric field values from all the pairs of voltage taps in the two legs are averaged to smooth out the inductance unbalances in the voltage taps readings. Representative values of electric field are thus obtained for the two sample legs (Equation 3.4.4).

$$E_{VHi}(\Delta t) = \frac{1}{N_{VHij}} \sum_{j=1}^{N_{VHij}} E_{VHij}(\Delta t) \tag{3.4.4}$$

With $E_{VHi}(\Delta t)$ the value of the electric field in the selected range Δt, associated to the average of the voltage sensor taps, generically indicated as $VHij$, with i generic index referred to the couples of sensors VH1/VH3 and VH2/VH4 in the two sample legs, and j referred to the four sensors in each couple (VH11/VH13, VH15/VH35, VH17/VH37, VH22/VH42, etc.). $N_{VHij} = 4$ is the number of voltage sensor couples, and $E_{VHij}(\Delta t)$ is the electric field in the selected range from the single voltage taps measurement.

The average electric field values are used for the representation of the V-I characteristics of the two CICCs in the selected range of current. To obtain the value of critical current and of the *n-index* for the sharpness of the transition, the power law (Equation 3.4.1) is interpolated to the data across the electric field criterion. Figure 3.4.3 shows representation of the V-I characteristics in logarithmic scale with the fit of the power law according to the equation:

$$y = C\left(\frac{x}{a}\right)^{b} \tag{3.4.5}$$

Substituting with C the electric field value at the criterion, and interpolating the characteristics to obtain I_c from the parameter a, and the n-value from the exponent b.

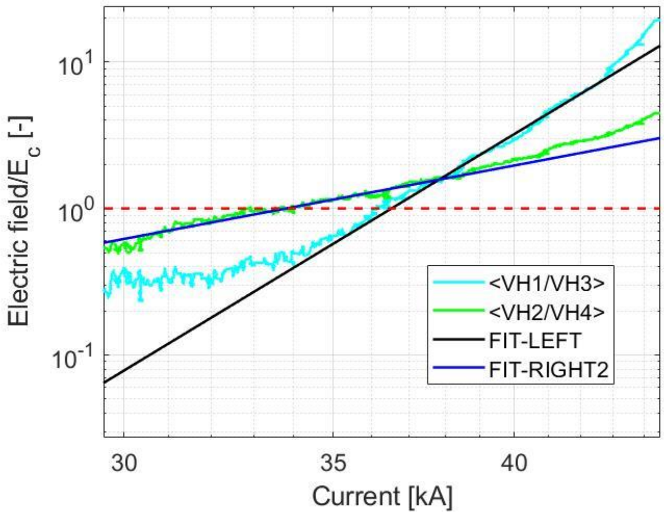

Figure 3.4.3: V-I transitions for critical current measurement test after WUCD at 3000 cycles. In black the result of the power-law interpolation in the left-leg, in blue the interpolation result in the right leg.

In some I_c measurements of the DTT TF test campaign, it was noticed the appearance of a second slope in the V-I transitions. In log-scale, the transitions showed a nonlinear behavior, particularly for electric fields above the criterion. In these cases, both the results of the two slopes have been accounted. From the processing of the measurements results (Section 4.3), it then emerged that the most reliable values where those from the interpolation of the power law across the criterion, with a best-fit of the electric field values just below and above the criterion. In Figure 3.4.4 is reported the V-I plot of the first I_c measurement test (before EM cycles). The nonlinear transition is evident in the right leg, with a pronounced slope above the criterion.

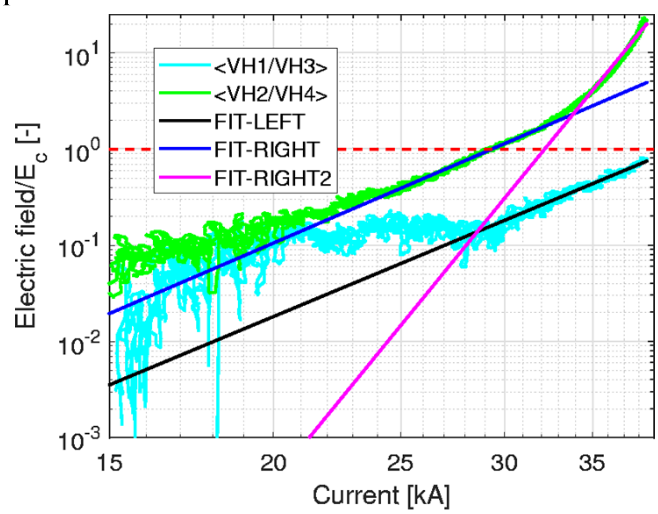

Figure 3.4.4: V-I transitions in the first I_c measurement test for the DTT TF samples. Evident nonlinearity in the right leg. The line in magenta shows the fit of the second slope appearing in the transition.

3.5 AC loss measurements tests

Over the T_{cs} and I_c measurement tests, which are generically referred as *DC Tests*, during the SULTAN test campaign of the DTT TF samples also transient AC measurement tests have been performed. The AC loss measurement tests are requested in any test campaign of superconducting magnets for fusion applications to estimate the energy deposition during transient plasma scenarios in operation. In several cases superconducting magnets must be either designed for pulsed operation (e.g. the central solenoid in a Tokamak) or must withstand transient changes of the self and background magnetic field (e.g. effect of a plasma disruptions, current instabilities in DC magnets, effects of the presence of pulsed magnetic fields from the AC operated central solenoid). In any case all superconducting magnets, whether designed for DC or pulsed operation, must be ramped to the operating condition. Thus, operation of a superconducting magnet is always associated to more or less severe conditions on the variation of the field seen by the cable [28]. Superconductors subjected to varying magnetic fields see multiple heat sources that can impact conductor performance and stability. Any field change produces energy dissipations that can be understood as emanating from the voltage induced in the conductor. The main energy loss terms are usually classified in *hysteresis* or *coupling* AC loss [8]. The hysteresis losses originate in the hysteretic nature of the magnetization in superconductors, when subjected to magnetic field cycles. Being associated to magnetization, they are volume dependent and are usually reduced with the employment of fine ($\sim 10\ \mu m$) superconducting filament wires in CICC cables. The coupling losses originate from cross currents between individual superconducting filaments separated by a copper matrix. When subjected to a transverse pulsed magnetic field, an electric field generates between the superconducting filaments inside each strand, and between the strands in the winding of the CICC cable. The electric fields generate cross currents in the copper matrix and resulting eddy currents flow through the inter-filaments and inter-strand copper matrix. These transient currents are associated to a characteristic time constant, the *coupling time constant* ($n\tau$), corresponding to the natural decay time of the eddy currents when the varying field becomes stationary [8].

To reduce the coupling losses in CICC cables the strands are chromium plated, twisted with an optimized twist pitch, and a steel foil is interleaved between the strand layers. These solutions increase the crossover resistance and so reduce the coupling currents, but on the other hand, can affect the cable stability. For stability, it is indeed necessary a higher compaction of the strands and a higher electrical contact to lower the differences of inductance between the strands and favor the current redistribution between wires. In case of a strand current saturation, the other wires can take on its current, avoiding a local transition and the formation of a normal zone in the CICC. For this reason, the cable design should account the AC losses, but always considering the trade-off with the stability aspects of the CICC conductor.

In SULTAN the AC loss characterization is assessed applying sinusoidal field pulses of fixed, small amplitude and variable frequency up to 2 Hz. The pulses are generated by the two saddle-shaped copper coils, placed around the sample in the high field zone of the SULTAN coils [13]. The generated effective field extends in a length of 390 mm along the sample. The testing parameters for AC measurements are selected to avoid the normal transition of the conductor sample and ensure that the coils during testing are not overheating. For this reason, a maximum power and pulse duration must not be exceeded. The maximum duration of the pulsed field depends on the field amplitude and on the SULTAN background field, which affects the dissipated power of the copper winding.

In the SULTAN test campaign for the DTT TF conductor samples, three blocks of AC measurement tests have been performed to test the possible effects of electromagnetic load cycles and thermal cycles of warm-up and cool-down on the AC losses generation. The first block of AC loss measurements was conducted at the begin of the test campaign, on the virgin TF conductor samples. The other block was done after the first 200 cycles, before the first WUCD, to test the loss reduction after plastic deformations due to EM forces and inter-strand movements. The last block of tests was after WUCD at 3000 EM cycles, to finally test the losses for the conductor at the end of the test campaign.

The main parameters of the AC loss measurement tests in the SULTAN test campaign for the DTT TF samples are reported in Table 6:

AC loss measurement	B SULTAN [T]	I sample [kA]	T Left [K]	T Right [K]	dm/dt L [g/s]	dm/dt R [g/s]	I pulse [A]	Pulse freq. [Hz]	Pulse duration [s]
Before cycles	2	0	4.5	4.5	5 – 2.5	5 – 2.5	±345sin	0.1 ÷ 2	20 – 30
After 200 cycles									
After WUCD at 3000 cycles									

Table 6: SULTAN parameters for the AC loss measurement tests of the DTT TF conductor samples.

The testing procedure in SULTAN for the AC loss measurements consists in triggering the field pulses in the inductive coils for the chosen pulse duration, with the specified frequency and amplitude. The pulses are triggered when the temperatures in the conductor samples are stable to the set-point values and, in case of subsequent pulses, when the inductive coil has cooled-down from the previous pulse. For the post-processing of the AC loss measurement tests, calorimetry is used to compute the *Loss-per-cycle* (i.e., the energy deposited in a single AC pulse period) for each pulse frequency test. In the calorimetric method it is assumed that all the heat generated by the pulse coils is transferred to the helium, whose change of enthalpy is quantified through the temperature sensors upstream (T_{in} *L*, T_{in} *R*, *T0L*, *T0R*, *T1*, *T2*) and downstream (*T3*, *T4*, *TX953*, *TX954*) the pulsed coil location along the sample (instrumentation scheme in Section 2.3). To define the thermodynamic state for the He enthalpy calculation, the corresponding closest pressure sensors are used (capillary *IN* and *OUT* pressure sensors in the right leg, and bench pressure sensors on the feeding lines of the two legs). For the enthalpy computation, the MATLAB package *matprop* [39] has been used. In the code, the NIST reference fluid thermodynamic properties for Helium [40] are employed.

In the present analysis, the calorimetric method has been applied from all the available temperature and pressure sensors measurements. During post-processing, it was then observed that the most stable and reliable results were from the enthalpies computed from the outlet pressures and the sensor-averaged temperatures downstream the inductive coil and close to it: sensors *T3* and *T4* in the two sample legs. All the other calorimetry results are less reliable due, for instance, to the conduction in the bottom joint termination. These results have been accounted as *errorbars* in the energy calculation, as the spread of the results due the different concurring instabilities or disturbances in the temperature and pressure sensors far from the inductive coil. In Figure 3.5.1 are reported the time evolutions of all the temperature and pressure sensors accounted for the application of the calorimetric method. The displayed results are from the first AC measurement test after WUCD at 3000 cycles, with a pulse frequency of 2 Hz.

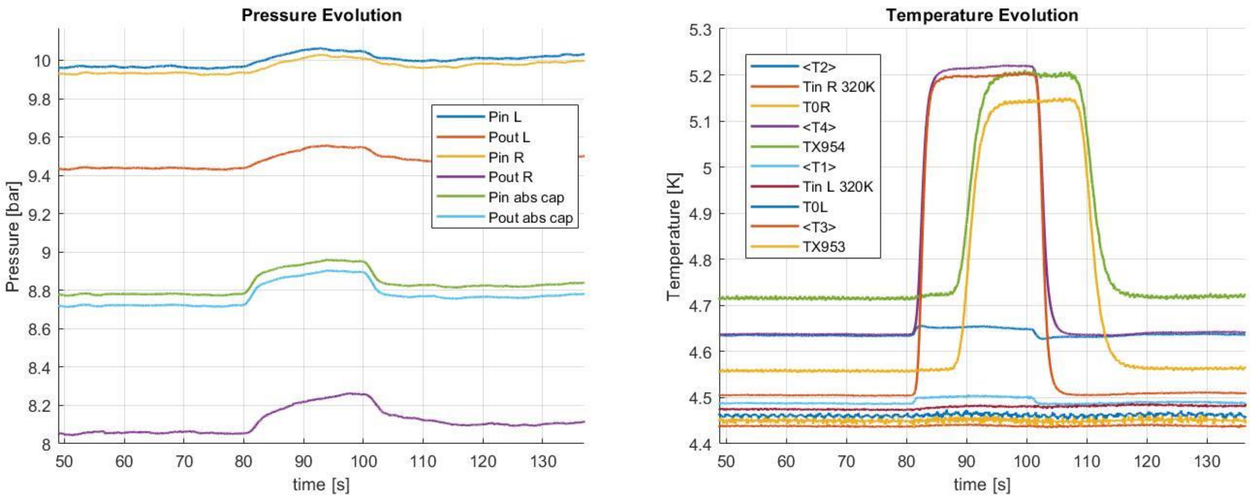

Figure 3.5.1: Pressure and temperature evolutions during the AC pulse at 2 Hz in the first test after WUCD at 3000 cycles.

The detailed calorimetry procedure employed in the AC losses measurement is here described. First, the enthalpies are computed from all the temperature and pressure sensors present in the two TF conductor samples, by means of the *matprop* package implemented in MATLAB. Their evolution is represented, and from visual inspection it is selected a suitable time interval in which the enthalpies are stable before the triggering of the pulsed AC field in the coils. In this interval, an averaging of the measured values is performed, and the resulting average enthalpies are subtracted to the correspondent values as a constant offset.

This is a fundamental step in the calorimetric method, since the energy deposition in the cable due to AC losses is accounted from the Helium enthalpy rise.

In Figure 3.5.2 the enthalpies computed from all the temperature and pressure sensors present in the two TF conductor samples are shown, at net of the average enthalpy measured before the AC pulses rigidly removed as an offset (underlined by a purple ellipse). The reported enthalpy evolutions are referred to the 2 Hz pulse in the above-mentioned AC test.

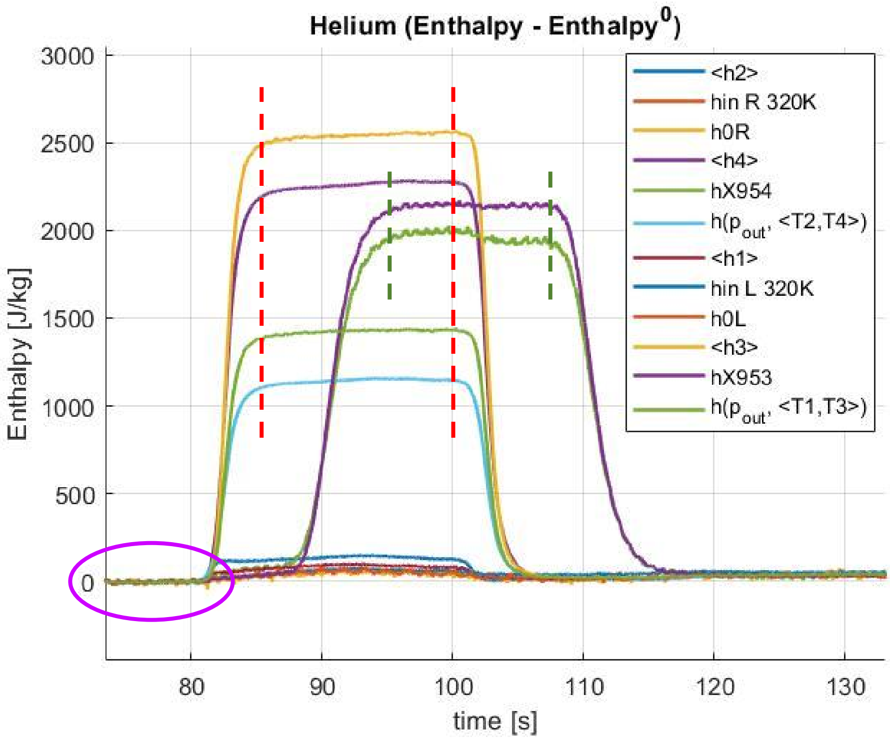

Figure 3.5.2: Evolution of the Helium enthalpy rise during the 2 Hz pulses for the test after WUCD at 3000 cycles. In purple the constant enthalpy interval for the offset removal is underlined. The vertical dashed lines define the intervals for the plateau enthalpy averaging in the application of the calorimetric method.

In the calorimetric method, the average power deposited from the AC pulse is obtained averaging the enthalpy rise in the relevant plateau interval in which the AC pulses are maintained. The average enthalpy rise is multiplied by the measured mass flow rate at the reference time instant before the AC pulses. In formula:

$$\dot{Q}_{dep} = \dot{m}(t_{offset})(\bar{h}_{plateau} - \bar{h}_{offset}) \quad (3.5.1)$$

With $\bar{h}_{plateau} - \bar{h}_{offset}$ the enthalpy rise computed as difference of the average enthalpy in the *plateau interval* and the average enthalpy in the *offset interval*.

The quantity of interest in the AC loss measurement tests is the *Loss per Cycle*, defined as the energy deposited in a single AC pulse of frequency ν. In a perfectly sinusoidal pulse, it is easily computed dividing the average power deposited to the frequency of the inductive coil pulses:

$$LossPerCycle = \dot{Q}_{dep}/_{\nu} \tag{3.5.2}$$

The obtained values of the *Loss per Cycle* are then reported in a plot as function of the pulse frequency and the results from the different AC measurements (before/after cycling and after WUCD at 3000 cycles) are compared for the assessment of the loss reduction with electromagnetic and thermal cycles.

A further characterization is then possible from the computation of the energy deposited in a single AC pulse. It is possible to retrieve the coupling and hysteresis loss contributions with a semi-analytical method based on the calculated Loss per Cycle [41]. The experimental assessment consists in retrieving the coupling loss time constant (nτ) and the hysteresis losses from the linear fit of the loss curve i.e., the Loss per Cycle vs. frequency, in the low pulse frequency range. In this range, the loss per cycle manifests a practically linear trend with frequency, thus a linear interpolation can be applied. In the procedure, the Loss per Cycle are normalized to the volume of the cable, computed from the effective cable cross-section and the length of the inductive field generated by the pulse coil along the sample ($L_{coil} = 390\ mm$) as reported in the following:

$$V_{cable} = (N_{strand} + N_{Cu})A_{strand}L_{coil}/\cos\theta \tag{3.5.3}$$

With $A_{strand} = \pi D^2_{strands}/4$ the area of a single strand and $\cos\theta$ the cosine of the twist angle of the cable. In the linear frequency range, the AC loss per unit volume can be approximated with a linear decomposition in a constant hysteresis loss term and a coupling term linearly varying with frequency.

$$loss\ per\ cycle = P'''_{hyst} + P'''_{coupling}(\nu) \quad \left[\frac{J}{cm^3}\right] \tag{3.5.4}$$

With P'''_{hyst} and $P'''_{coupling}$ the loss contributions per unit volume of the cable.

From the interpolation of the loss curves in the low frequency range (0.1÷0.5 Hz) with a generic linear function:

$$y = a + bx \qquad (3.5.5)$$

It is possible to obtain the hysteresis loss contribution from the intercept a, and the characteristic time of coupling currents (which is the relevant parameter in the coupling loss assessment) from the slope b. To retrieve the $n\tau$ parameter from the linear slope of the fit, a simplified analytical model for the evaluation of the coupling losses is employed [42]. In this model the screening-currents effects are neglected, and the small oscillation approximation for a sinusoidal field sweep perpendicular to the cable axis is used. The simplified equation from [42] is reported:

$$P'''_{coupling} = \frac{\Delta B^2 \pi \omega n\tau}{\mu_0} \qquad (3.5.6)$$

With $\Delta B = 0.3\,T$ the peak-to-peak amplitude of the pulsed magnetic field generated by the inductive coil, $\omega = 2\pi\nu$ is the angular frequency of the sinusoidal pulse and μ_0 is the magnetic permeability of vacuum. By inversion of equation (3.5.6) obtained the coupling time constant $n\tau$ is finally.

$$n\tau = \frac{P'''_{coupling}}{\nu} \frac{\mu_0}{2\pi^2 \Delta B^2} \qquad (3.5.7)$$

With $\frac{P'''_{coupling}}{\nu} = b$, the slope of the linear fit interpolation. The results of these calculations will be presented in the dedicated section of the following Results chapter (Section 4.5).

3.6 Minimum Quench Energy (MQE) measurement tests

At the end of the SULTAN test campaign for the DTT TF conductor samples, the conductor *energy stability margin* has been assessed through tests of fast transient electromagnetic pulses: the tests of Minimum Quench Energy (MQE). The goal of these tests is to obtain the minimum energy necessary to *quench* the conductor, so to generate a transition from the superconducting state to the normal conducting state. When a thermal perturbation (heat deposition from different possible sources, as described in Section 3.3) generates a normal state transition in a superconducting magnet, two possible consequences can result. If the heat deposited and generated by Joule heating in the current sharing regime do not overcome the heat removal from the supercritical helium flow in the CICCs, the *recovery* of the conductor occurs. If instead, the heat removal cannot overcome the deposited power and no other mechanisms (e.g., the *quench protection system*) can prevent the transition to the normal conducting state, the temperature in the normal zone increases further and the normal front propagates, so that the superconductor experiences an irreversible process leading to the complete loss of superconductivity in the magnet i.e., the magnet experiences a *quench* [28].

For the consequences of a quench event in the magnet system of a superconducting fusion reactor, the assessment of the minimum quench energy and the adoption of quench protection systems to reduce the damages from such events, are of prior importance in the fusion magnet system design. Still today, despite the progresses in understanding the concurring phenomena and the improvements in the manufacturing techniques, stability remains one of the limiting factors for high performance magnets. In superconducting magnets, an *energy margin* can be defined as the minimum energy density that the external source needs to provide to the cable to cause a thermal runaway. An energy input larger than this, causes a thermal runaway, while a smaller energy input leads to a recovery. For perturbations of known and limited distribution in space it is usually referred to the *minimum quench energy* (MQE) that corresponds to the integral in space of the energy margin and is thus measured in Joule units.

In SULTAN, the MQE tests for the DTT TF conductor samples are carried out at nominal current but with a reduced field of 9 T, to avoid damages in the inductive pulsed coils (the same used in the AC tests) when triggering a quench. The tests are repeated at different testing temperatures starting from the maximum value of $T_{cs} - 0.1\ K$, to test the quench behavior at different temperature conditions. The inlet temperatures in the MQE tests are slightly lower than the T_{cs} measured in the corresponding electromagnetic conditions (reference T_{cs} run at 9 T and 42.5 kA), in order to trigger a (unrecoverable) normal state transition with a fast pulse, since the conductor is maintained at the nominal current, so just below the critical surface (recalling the T_{cs} definition).

To induce a normal transition that possibly results in a thermal runaway, fast single AC pulses are generated by the inductive coils, discharging the current from the battery of capacitors (*pulse-battery*) connected to the inductive coils [13]. The battery is charged before each pulse-trigger with consecutively increasing voltage, from a minimum of 100 V up to the voltage level required to cause the quenching of the conductor sample, using steps of 20 V. A test run without current in the sample is performed after the MQE current runs. This test is commonly called *calibration run*, and it is the essential test for the MQE calculation: from this test is possible to compute the energy deposited in the sample due to the pulse of minimum voltage which triggered the quench in one or more current runs, by applying *calorimetry*. It is hence possible to retrieve the minimum quench energy without the bias of AC induced losses in the conductor and/or normal transition recovery which necessarily generates additional power in the conductor when tested with current. The main parameters of the SULTAN tests of minimum quench energy for the DTT TF conductor samples is reported in Table 7.

MQE Tests	B SULTAN [T]	I sample [kA]	T Left [K]	T Right [K]	dm/dt L [g/s]	dm/dt R [g/s]	Pulse coil voltage [V]
Calibration Run	9	0	8.33-0.1 K	7.87-0.1 K	2.5	2.5	100/120/140/160
Current runs		42.5	8.33-0.1 8.33-0.3	7.87-0.1 7.87-0.2 7.87-0.3 5			100/150 100/120/140 140 100/120/140 100/120/140/160

Table 7: SULTAN MQE test parameters for the DTT TF conductor samples.

As it will be discussed in the dedicated section in the results chapter (Section 4.6), some issues resulted from the MQE testing for the DTT TF-B sample. In all the current runs of the MQE tests, the TF-B (right leg) conductor manifested a quench with pulses around 140 – 160 V, independently on the inlet temperature set-point. Even with the tentative minimum temperature of 5 K the quench was initiated in this leg at the same pulse voltage. It was hence not possible to measure the MQE for the TF-A (left leg) in the SULTAN test campaign. Different hypotheses have been advanced for the quench behavior of the right leg sample. Possible damages in a strand or a group of strands can cause the formation of a local normal zone which then propagates up to the thermal runaway of the conductor. This is however inconsistent with the found results of T_{cs} *and Ic*. Another hypothesis is a possible criticality in the heat removal which causes the formation of a local hotspot, subsequently propagating and causing the conductor quench. This can be also thought to take place in some strands in proximity with the observed obstruction in the inlet region of the TF-B conductor sample. Speculations can be made on the origin of this unexpected quench behavior of the TF-B conductor, but it cannot yet be assessed confidently from the analyses presented. On this, a final word will probably come from the destructive inspection of the sample that will be done by ENEA in the forthcoming weeks.

In the present work however, a calorimetry analysis has been accomplished to assess the minimum quench energy in the TF-B conductor. The calorimetric method employed here is similar to that described in the AC loss measurement tests. The enthalpy is computed with the *matprop* package implemented in MATLAB [39], from the sensor-averaged temperature measurements from sensors T3, T4 downstream the inductive coil, and from the outlet pressures in the two sample legs. Calorimetry was applied also in the TF-A sample to check if the energy deposited in this leg showed some differences with the TF-B sample.

Differently from the calorimetry applied in the AC loss measurements, here the enthalpies are computed just from the temperature and pressure sensors downstream the inductive coil position, being more reliable than the measurements from sensors at higher distance to the inductive coil, particularly when a single pulse is induced in the conductor. Also, the approach to the calculation of the enthalpy rise is different than in the AC loss measurements. The offset here removed is not constant but linear in those pulses in which temperature instabilities are superimposed to the actual temperature rise due to the fast discharge in the inductive coil. Figure 3.6.1 shows the enthalpy evolutions from the sensor-average temperatures and outlet pressures for the left and right leg, during the pulse at 140 V in the calibration run. The black dashed lines show the linear offset applied for the computation of the enthalpy rise.

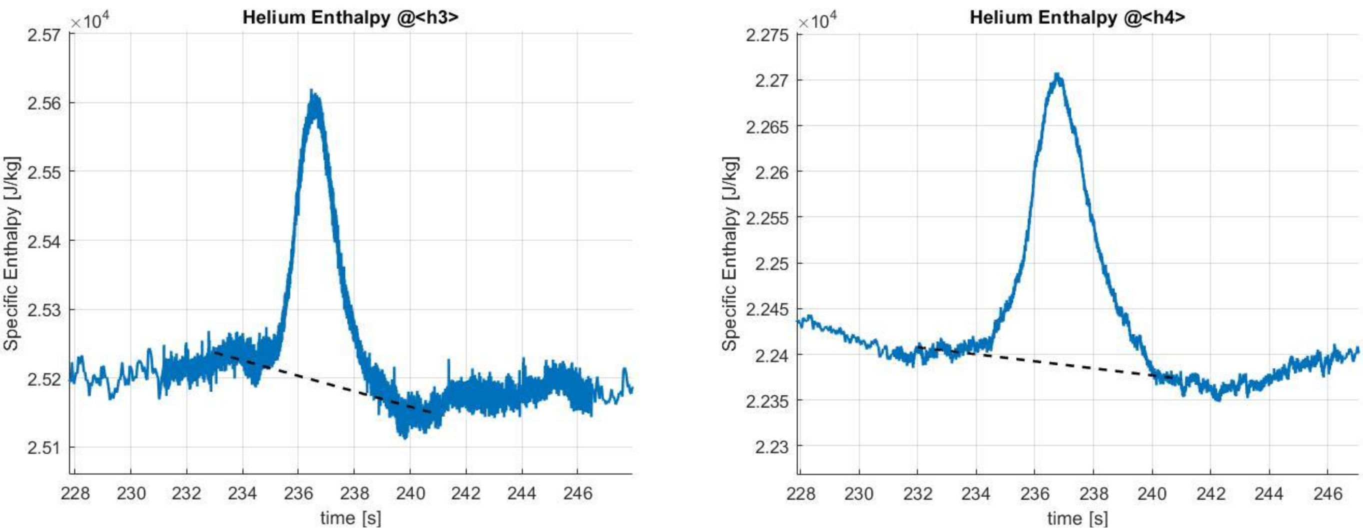

Figure 3.6.1: Evolution of the Helium enthalpies in the left and right leg during the 140V pulse in the calibration run. In black the linear offset to be subtracted to correctly define the temperature rise.

The linear offset is then subtracted from the calculated enthalpies in the time interval of the pulsed discharge, to compute the enthalpy rise from the energy deposited by the inductive coil. In Figure 3.6.2 the obtained enthalpy rises for the 140V discharge are shown.

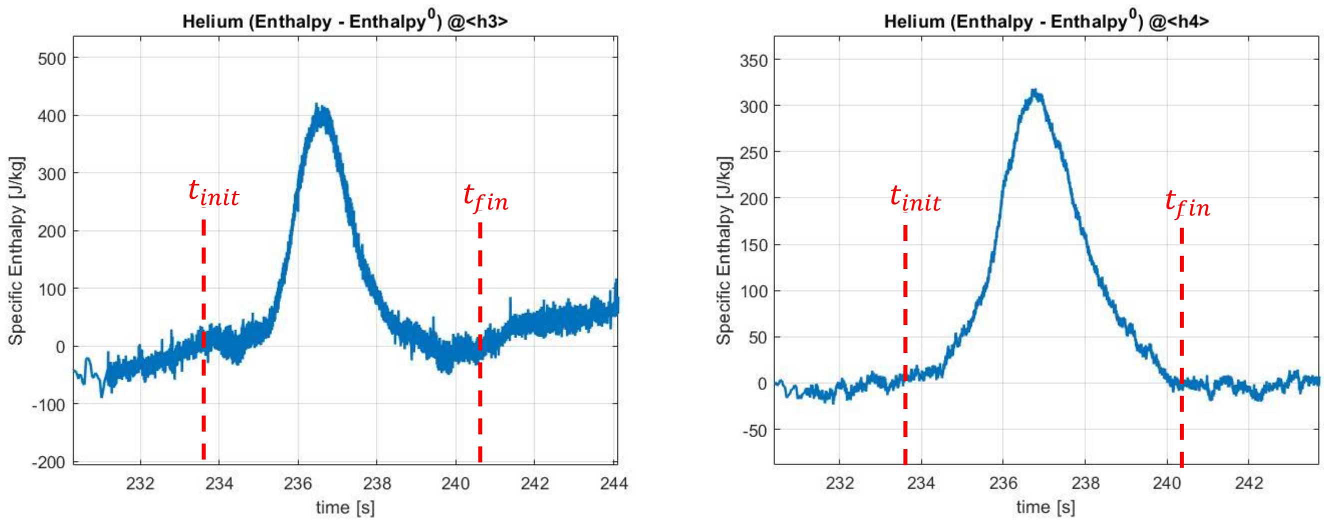

Figure 3.6.2: Enthalpy rise evolution for the left and right leg during the 140V pulse in the calibration run. Linear offset removed to correctly determine the pulse heat deposition. Red dashed lines for the integration interval definition.

For the calorimetry assessment of the deposited energy in the conductor from the AC pulse generated in the inductive coil, the enthalpy rise is integrated with the trapezoidal method (built-in MATLAB function *trapz* [36]) in the time interval around the enthalpy rise. The interval definitions for the 140V pulse for the left and right leg enthalpy increases are underlined with the vertical red lines in Figure 3.6.2. In this interval, the integration is performed, and the energy deposited in the helium due to the AC discharge is obtained multiplying by the mass flow rate at the reference time instant at the begin of the pulse, according to the calorimetric method. In formula, the resulting equation for the deposited energy computation is here reported:

$$Q_{dep} = \dot{m}(t_{init}) \int_{t_{init}}^{t_{fin}} [h(t) - h^0(t)]dt \tag{3.6.1}$$

With $h(t) - h^0(t)$ the enthalpy rise calculated subtracting the linear offset $h^0(t)$ in the relevant time interval $[t_{init},\ t_{fin}]$. The desired value of the MQE is then obtained from the deposited power at the minimum voltage at which quench has been observed in the current runs.

4. Analysis of the experimental data

4.1 Pressure drop characterization

The results of the pressure drop characterization tests on the TF-B conductor sample are here reported. The results are presented as described in Section 3.2: the characterization of the measured pressure drop is normalized to the length between the pressure capillaries to rescale the result obtained on the sample to the DTT TF coil, for the design and dimensioning of important components of the cryoplant (e.g., the vacuum pumps). Figure 4.1.1 shows the obtained hydraulic characteristics for the two tests at the begin of the cycles (BoC) and at the end of cycles (EoC). The results are presented both with and without the pressure offset removed at zero mass flow rate. A parabolic fit of the results at EoC was used to remove the offset and shows good agreement with the measured data. The results at BoC do not clearly follow a parabolic dependence on the mass flow rate. The presence of the obstruction limited the maximum reachable mass flow rate (at 100% valve opening) and due to the high associated pressure drop, it generated a He temperature rise.

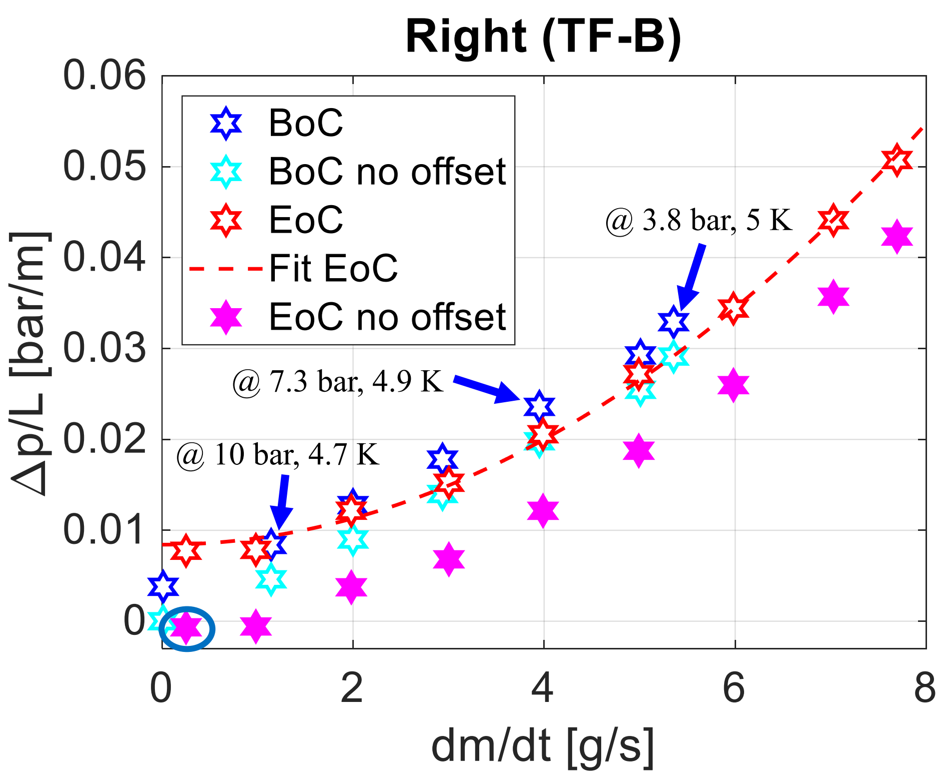

Figure 4.1.1: Hydraulic characteristics of the TF-B resulting from the pressure drop characterization tests. In red, the parabolic interpolation of the pressure characteristic at EoC.

The blue arrows in Figure 4.1.1 marks some of the points of the hydraulic characteristic at BoC, showing the reduction of the inlet capillary sensor pressure reading and the temperature increase up to 0.5 K from the initial temperature set-point value. Due to the mentioned phenomena related to the presence of the flow obstruction we can conclude that some criticality resulted on the measured pressure drop values at BoC, questioning their reliability. The light-blue circle in the first point of the EoC characteristic is placed to remark that the first measured point is not reliable due to high pressure and mass flow oscillations. Apart from the first point, the EoC characteristic shows the expected parabolic trend and a reduction of the measured pressure drop of a factor of ~ 2 at the nominal mass flow rate (4 g/s).

The results of the comparison of the friction factor computed from the measured data with the correlations mentioned in Section 3.2 as function of the Reynolds number are displayed in Figure 4.1.2.

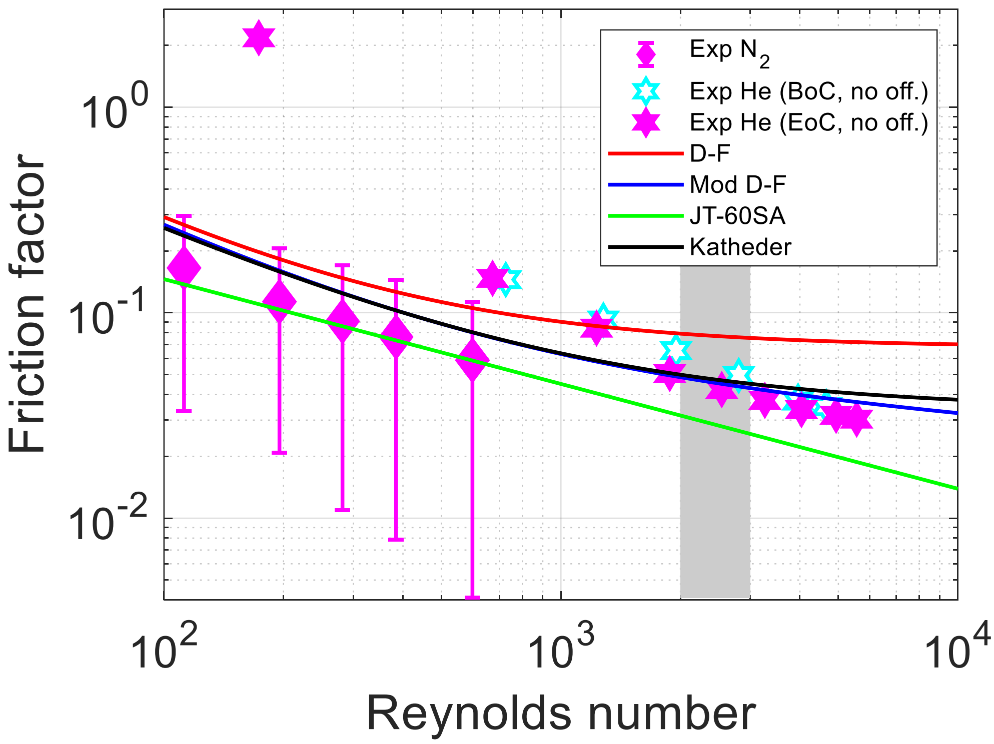

Figure 4.1.2: Comparison of the friction factor vs. Reynolds number from measured data with the mentioned correlations for CICC cables.

In the comparison, also the measured data from the hydraulic testing of a Cu-dummy sample of the DTT TF conductor have been included [12]. The results of the tests performed with N_2 gas at room temperature are however out of the relevant range for the operation with supercritical Helium. The errorbars are due to the use of inlet or outlet pressure data for the density evaluation. The resulting friction factor values from the measured data show good agreement with the modified Darcy-Forchheimer correlation [25] at the nominal mass flow rate (4 g/s). Particularly, the value at EoC is perfectly captured by the Mod D-F correlation. This is a relevant result for the numerical thermohydraulic analyses, since this correlation has been used so far in the 4C code for the thermohydraulic characterization of the DTT TF magnet system [23].

4.2 Tcs measurements

The analysis of the current sharing temperature measurement tests discussed in Section 3.3, is here presented. The two main outcomes of these tests: the current sharing temperature and the broadness of the normal state transition (*m-index*), are presented for the tests at nominal effective magnetic field and current as function of electromagnetic cycles. The results from the two possible slopes for the fit of the power-law for the V-T characteristics (Equation 3.3.3) are considered. For the two sample legs (corresponding to the TF-A and TF-B conductors) the obtained T_{cs} values at the different EM and thermal cycles are displayed in Figure 4.2.1. The black arrows clarify the measurements after thermal cycle of warm-up and cool-down of the samples. The measurement at 500 EM cycles for the right leg conductor (TF-B) is circled in green to underline that it is the result of a not reliable measurement. In this test, the thermal runaway in the left leg prevented to reach the electric field criterion in the right leg, so the measured T_{cs} value is actually the result of an extrapolation from the power law.

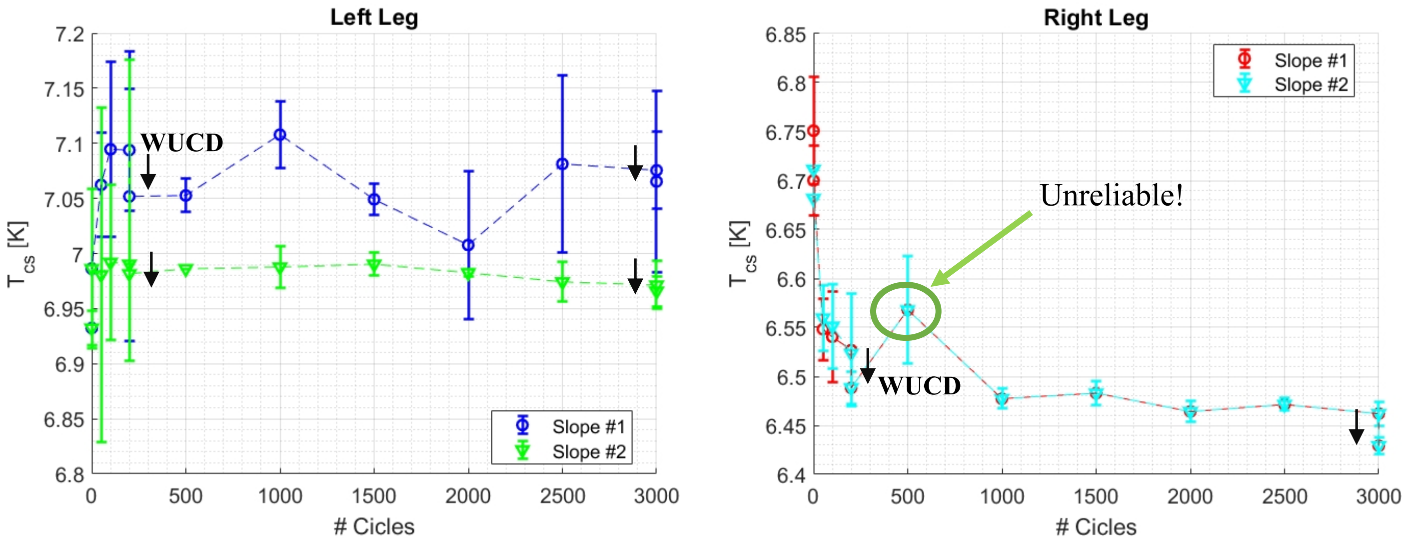

Figure 4.2.1: Measured T_{cs} values vs, number of electromagnetic cycles. Black arrows show the effect of the thermal cycles.

From the T_{cs} results for the left leg conductor, which is the one more affected by the 'double slope phenomenon', it is clear how the best-fit of the points of the V-T characteristics across the 10 $\mu V/m$ criterion gives the most stable results. The second slope interpolation can be considered more suitable for the T_{cs} experimental assessment because of the higher reliability of an interpolation across the criterion compared to an extrapolation, for the weaker dependence of the V-T points on the voltage offset removal during the data reduction, and also because it gives more conservative results, providing lower T_{cs} values compared to the first slope interpolation. In the right leg, the double slope in the V-T transitions is present just in the T_{cs} measurements at 0 and 50 EM cycles. For this leg the T_{cs} values appears almost stable after WUCD at 200 EM cycles. In figure are reported also the errorbars from the confidence intervals of the fit of the power law. It must be noted that being the result of a numerical fit, the errorbars depend strongly on the number of available points, rather than being representative of the actual inaccuracy on the measurements. So, they must be considered as result of the fit of the V-T characteristics with the power law. An analogue analysis is performed for the broadness of the temperature-transition to the normal conducting state. The parameter defined as *m-index* is used to describe the sharpness (or broadness) of the transition for the V-T characteristics. The result of the analysis of this parameter with EM and thermal cycles is reported in the following Figure 4.2.2.

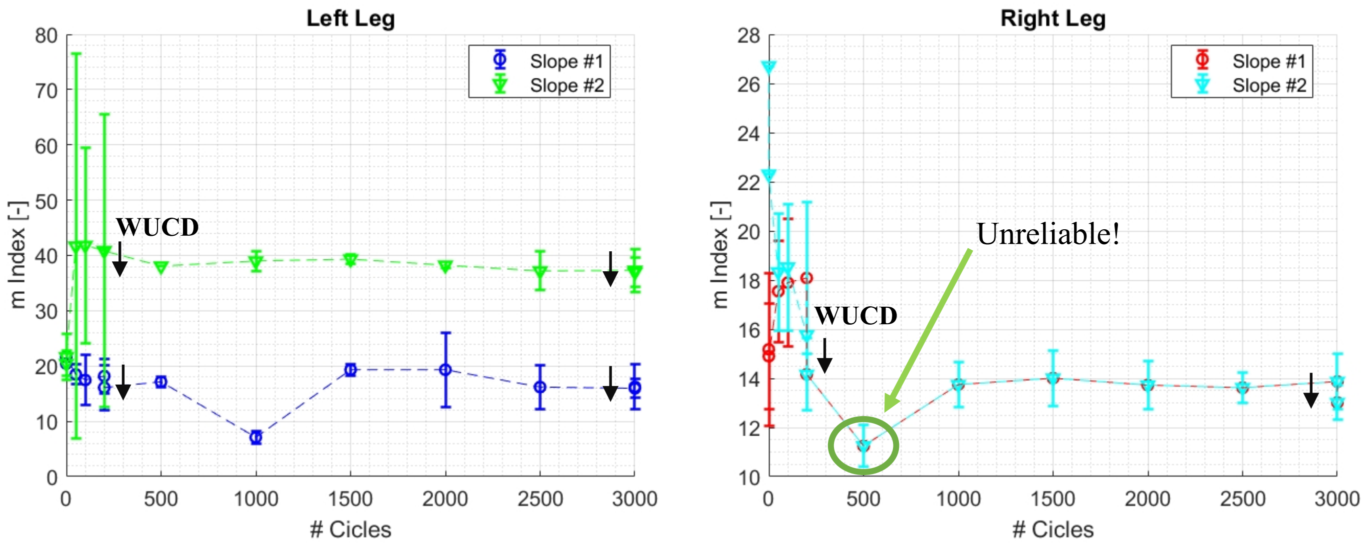

Figure 4.2.2: m values vs, number of electromagnetic cycles. Black arrows show the effect of the thermal cycles.

As for the T_{cs} results vs. cycles, also for the *m-index* in the left leg the most stable results come from the fit with the second slope, crossing the criterion. In the right leg, apart from the point at 500 EM cycles which is judged unreliable, as previously said, the *m-index* is almost stable after WUCD at 200 cycles. Also here, the reported errorbars results from the confidence intervals given from the fit of the power law, so they are not necessarily representative of the actual inaccuracy.

In Table 8 are resumed the obtained results of the T_{cs} measurements, for the tests at nominal electromagnetic load conditions. From the T_{cs} values for the left leg (TF-A) it can be concluded that no evident signs of degradation on the current sharing temperature have been measured in the 3000 EM cycles and two WUCD. The T_{cs} remained stable around ~ 7 K and a slight improvement was measured after the first 50 EM cycles. For the broadness of the transition in the left leg, after an initial sharpening with the first 50 EM cycles, the *m-value* remained almost stable around 40, with a slight decrease (increase in the broadness of the transition) in the last 1000 EM cycles and one WUCD. In the right leg, instead, degradation on the T_{cs} has been observed after the first 50 cycles, with a reduction of ~ 0.2 K, and with the thermal cycles, which reduced again the T_{cs} of ~ 0.1 K. The final measurement gave a T_{cs} value for the right leg (TF-B) of ~ 6.4 K. Also the *m-index* in the right leg experienced a decrease with cycling, decreasing up to 13 after the WUCD at 3000 cycles.

	Tcs [K] – Slope#2		m-value [-] – Slope#2	
EM cycles	Left leg	Right leg	Left leg	Right leg
0	6.93	6.71	21	27
50	6.98	6.56	42	18
100	6.99	6.55	42	18
200	6.99	6.52	41	16
200 (WUCD)	6.98	6.49	41	14
500	6.99	6.56	38	11
1000	6.99	6.48	39	14
1500	6.99	6.48	39	14
2000	6.98	6.46	38	14
2500	6.97	6.47	37	14
3000	6.97	6.46	37	14
3000 (WUCD)	6.97	6.42	37	13

Table 8: Summary of the results of T_{cs} measurements at nominal EM load, for the different EM and thermal cycles. Measurement at 500 EM cycles for the right leg unreliable (marked in red).

It is known that in Nb3Sn CICCs the degradation of properties versus load cycles can be attributed to plastic deformation of the Nb3Sn strands or fracture of the superconducting filaments. This degradation can be expressed in a reduction of T_{cs} or I_c, but as found in [31], a more sensitive parameter for the assessment of degradation of the Nb3Sn strands is the increase of the broadness of the transition to the normal conducting state. The increased broadness of the transition translates in a reduction of the *m-index*, which is what has been seen in both the TF conductor samples, but particularly in the TF-B.

So, a slight degradation with cycles have been experienced by both the tested TF samples. However, being the TF a DC operated coil, the obtained results in terms of degradation are satisfactory, since it will never experience high numbers of EM cycles and also few thermal cycles during operation.

For what concerns the stability of the conductors, from the obtained T_{cs} values at the end of cycles (~ 7 K in the left leg, ~ 6.4 K in the right leg), the design minimum temperature margin of 1.4 K is overcome by both the conductor samples. The obtained margin is increased of ~ 1.1 K in the left and ~ 0.4 K in the right, so the requirement is satisfied.

4.3 I_c measurements

The results of the critical current measurements tests are reported for the tests at nominal field as function of the electromagnetic and thermal cycles after which they have been measured. As it was said in Section 3.4, in SULTAN test campaigns the V-T characteristics are preferred for the evaluation of normal-state transitions and the related effects on conductor degradation. However, important results can be obtained also from the evaluation of critical current measurements when the test conditions allow a fair comparison between the obtained results. For a more reliable comparison between the obtained I_c results after EM and thermal cycles, it is fundamental that the testing temperature of $T_{cs} + 0.4\,K$ is the same in all measurements. Thus, a reference T_{cs} temperature measurements must be considered in all I_c results. From the testing temperatures employed in the I_c runs for the DTT TF conductors, a fair comparison on the I_c results is possible from the measurement test after WUCD at 200 EM cycles onwards. In Figure 4.3.1 are reported the I_c measurements as function of electromagnetic and thermal cycles. The thermal cycles are marked with the black arrows. The presented results are from the two power law interpolations, at lower and higher current (‘first’ and ‘second’ slope) when the presence of a double slope was evident in the V-I transition. However, the more reliable results are from the power law interpolation better fitting across the electric field criterion.

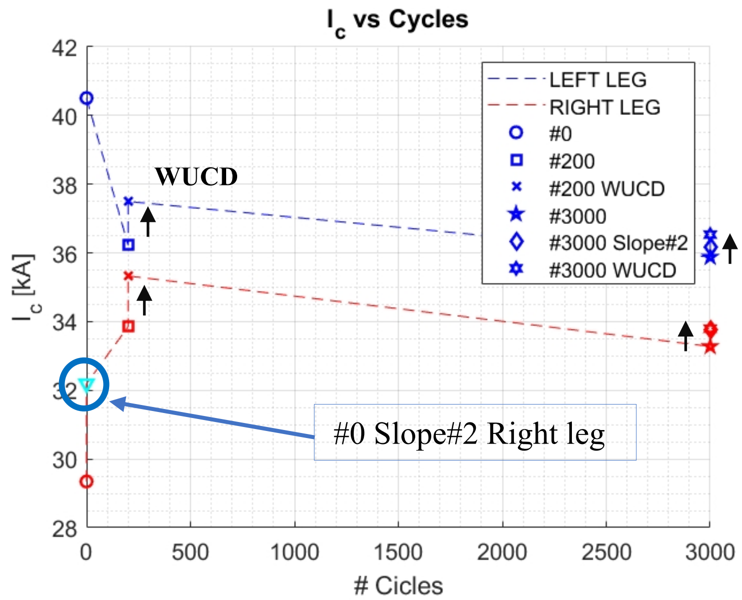

Figure 4.3.1: Ic measurements vs. EM and thermal cycles. The black arrows underline the thermal cycles. Results with the second slope only for the measurements at 0 and 3000 EM cycles.

As shown in Figure 4.3.1, for the results at the same testing temperature (from the measurement after WUCD at 200 EM cycles), a slight reduction of the critical current with cycling is observed with a final improvement in the last measurement, after WUCD at 3000 EM cycles. In Figure 4.3.2 are shown the values of the sharpness of the transition (*n-index*) at the different EM and thermal cycles. Also for the *n-index* a slight variation with cycles is observed for the comparable results. Considering the second slope in the test after WUCD at 3000 cycles a reduction of the sharpness of the transition is observed, differently to what observed for the *Ic*.

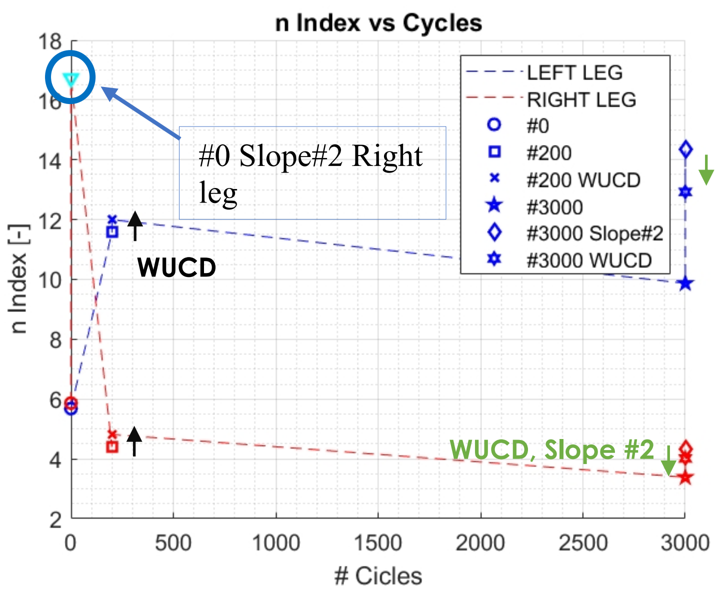

Figure 4.3.2: n-index vs. EM and thermal cycles. The black arrows underline the thermal cycles. Results with the second slope only for the measurements at 0 and 3000 EM cycles.

In the reported figures of I_c vs. cycles and n-index vs. cycles (Figure 4.3. and Figure 4.3.2) the errorbars from the fit have not been included. As for the T_{cs} measurement tests, the errorbars results from the confidence intervals of the best-fit of the power law. They are strongly dependent on the number of points used for the interpolation. In The case of the V-I characteristics, all the electric field values in the chosen current interval have been employed for the fit, as described in Section 3.4. Due to the large number of points used for the fit, the errorbars are less than ±1% for both I_c and the n-values, so they have not been displayed in the reported plots.

In Table 9 are reported the results of the critical current measurements for the DTT TF conductor samples. The results are from the interpolation of the slope crossing the electric field criterion. Apart from the measurement at 3000 EM cycles in which the second slope is used, in all other measurements the results are from the first slope interpolation. The measurement at reduced SULTAN field of 10 T is reported in the last row: for the different applied field, this cannot be compared with the other reported measurements.

	Ic [kA] – Slope#1		**n-value [-] – Slope#1**	
EM cycles	Left leg	Right leg	Left leg	Right leg
0	40.5(@7.1K)	29.3(@7.5K)	5.7	5.9
200	36.2(@7.4K)	33.8(@6.9K)	11.9	4.5
200(WUCD)	37.5(@7.3K)	35.3(@6.8K)	11.9	4.8
3000	36.2(@7.3K)	33.8(@6.8K)	14.3	4.3
3000 (WUCD)	36.5(@7.3K)	33.8(@6.8K)	12.9	4.0
Measurement at 10 T after 3000 cycles and WUCD	35.8(@8.0K)	34.2(@7.5K)	11.3	4.7

Table 9: Summary of the results of I_c measurements at nominal EM load, for the different EM and thermal cycles. Last measurement at reduced field. In brackets the testing temperatures for the left and right leg. Measurement at 0 EM cycles unreliable due to the mistaken testing temperatures for the two legs.

Analyzing the comparable results of I_c measurements (from the run after WUCD at 200 cycles), it can be noticed a slight reduction on the I_c in the two legs from the run after WUCD at 200 cycles and the run after 3000 cycles. After the WUCD at 3000 cycles, the I_c appears stable in both legs. The found I_c values in this last run at full load are equal to 36.5 kA in the left leg, and 33.8 kA in the right one. Concerning the sharpness of the transition (*n-index*), in the left leg a slight increase in the run at 3000 cycles is observed, with a successive reduction to a value of ~ 13. In the right leg, the *n-index* decreases in the comparable results up to a value of 4.

4.4 T_{cs} measurements at different EM loads: strain analysis

As described in Section 3.1 and Section 3.3, in the SULTAN test campaign of the DTT TF conductor samples, T_{cs} measurements at different EM loading conditions have been performed after the WUCD at 3000 nominal load EM cycles. The fundamental aims of these tests were the reconstruction of the operation space of the conductor and the analysis of the effective strain behavior at different EM loads [18]. For the operation space reconstruction, the T_{cs} results are represented as function of the testing currents in the sample (Figure 4.4.1). This representation suggests the increase of the current sharing temperature, so of the temperature margin, at reduced currents and magnetic fields. As for the other T_{cs} tests, the results are obtained from the best-fit of the second slope with the V-T power law.

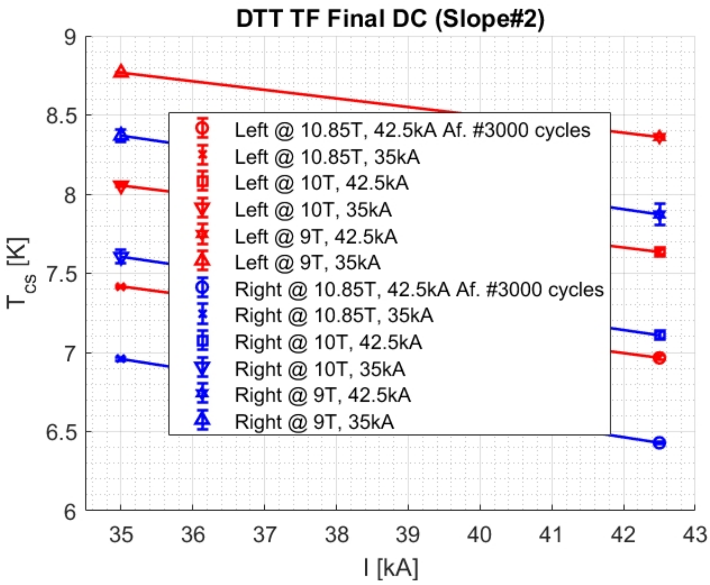

Figure 4.4.1: T_{cs} vs. testing current sample for the two DTT TF conductors. The lines connect the points tested at the same SULTAN field.

The T_{cs} measurements results are reported also in the following Table 10, for the different electromagnetic loads. All measurements have been conducted after WUCD at 3000 EM cycles at the full EM load (10.85T x 42.5kA).

	Tcs [K] – Slope#2		**m-value [-] – Slope#2**	
EM Load	Left leg	Right leg	Left leg	Right leg
10.85T, 42.5kA	6.97	6.42	37	13
10.85T, 35kA	7.42	6.96	41	15
10T, 42.5kA	7.63	7.11	44	15
10T, 35kA	8.05	7.60	47	19
9T, 42.5kA	8.36	7.87	51	20
9T, 35kA	8.76	8.37	55	24

Table 10: Summary of the results of the T_{cs} measurements at different EM loads. The first run reported is the test at nominal EM load after WUCD at 3000 cycles.

As evident from the results in table, the T_{cs} values are increased of ~ 2 K at 9 T and 35 kA compared to the T_{cs} run at nominal load (10.85T x 42.5kA) after WUCD at 3000 EM cycles. Also the broadness of the transition varies with the applied EM load, showing an increase of the *m-value*, so a reduction of the broadness of the transition compared to the same T_{cs} run at nominal load.

A fundamental analysis carried out from the T_{cs} measurements at different loads is the conductor *strain characterization*. The *total effective strain* can be calculated from the fit of the measured T_{cs} at the correspondent *effective magnetic field*, as function of the electromagnetic load (I x B). The total effective strain is a lumped parameter made up of three contributes [43]:

$$\varepsilon_{total} = \varepsilon_{CD} + \varepsilon_{crush} \tag{4.4.1}$$

With ε_{CD} the compressive thermal strain (cool-down strain) due to the cooling of the sample from the preparation temperature (650°C for Nb_3Sn) to 4.5 K, ε_{crush} the compressive strain from the transverse EM forces crushing the cable against the wall of the jacket during the current operation with transverse magnetic field.

In the full magnet coil in operation (e.g., the DTT TF coil), another strain contribution is the hoop strain, ε_{hoop}: the tensile longitudinal strain acting on bended conductors during current operation due to EM forces (hoop tensile strain). This contribute is not accounted on the considered SULTAN DTT TF samples since they are straight conductors, so not subjected to tensile hoop forces. This leads however to conservative calculations of the effective strain since the neglected contribution is of tensile strain: usually improving the performances and increasing the T_{cs} [43].

The effective total strain is calculated with a simplified model [43], without considering the complex strain spatial distribution. In the model, the temperature, current and strain distributions are assumed to be uniform in the cable cross section. The effective strain is found with an iterative procedure up to convergence of the T_{cs} calculated from iterative inversion of the strand current characterization [44], described in Appendix A.1, to the measured T_{cs} value.

$$J_c(T_{cs}, B_{eff}, \varepsilon_{total}) \tag{4.4.2}$$

Equation 4.4.2 recalls the functional dependences of the strand current characterization used in the iterative procedure. Among the dependences, the effective magnetic field B_{eff} must be considered. The calculation procedure of the effective magnetic field from the spatial distribution on the cable cross section is described in Appendix A.2. Figure 4.4.2 shows the resulting values of effective total strain as function of the applied electromagnetic loads.

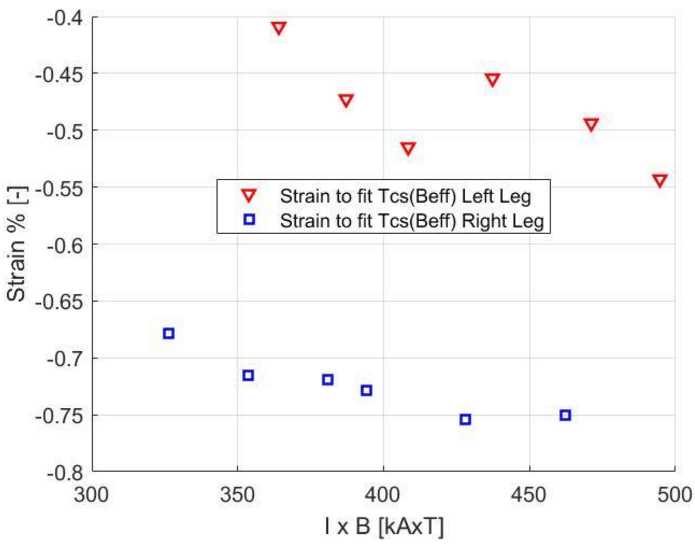

Figure 4.4.2: Effective Total Strain vs. applied electromagnetic load for the two TF conductor samples.

The results show a lower compressive total effective strain in the left leg (TF-A), with maximum compressive value of -0.55%. In the right leg, higher compressive strain values are observed, with a maximum value of -0.75%.
From the strands data given in [44], it is known that the value of thermal cool-down strain is equal to $\varepsilon_{CD} = -0.356\ \%$, thus in the highest EM loading conditions the maximum values of the compressive crushing strains (ε_{crush}) in the two legs are equal to ~ -0.19% for the left leg, and ~ -0.39% for the right leg. To these maximum compressive strains are associated the reported values of current sharing temperature at 10.85T and 42.5kA (measurement after WUCD at 3000 EM cycles in Table 10).

4.5 AC loss measurements

The results of the AC loss measurement tests described in Section 3.5 are resumed in the plot of Figure 4.5.1. The Loss per Cycle are displayed as function of the pulse frequency, defining the loss curves for the three blocks of tests at begin of EM cycles (BoC), after 200 EM cycles (reported as end of cycles, EoC), and after thermal cycles of WUCD. The marked data on the loss curves results from the calorimetry on the sensor-averaged temperatures from T3 and T4 on the two sample legs, and from the available outlet pressures. The errorbars are from the results of calorimetry calculations on the other temperature and pressure sensors available.

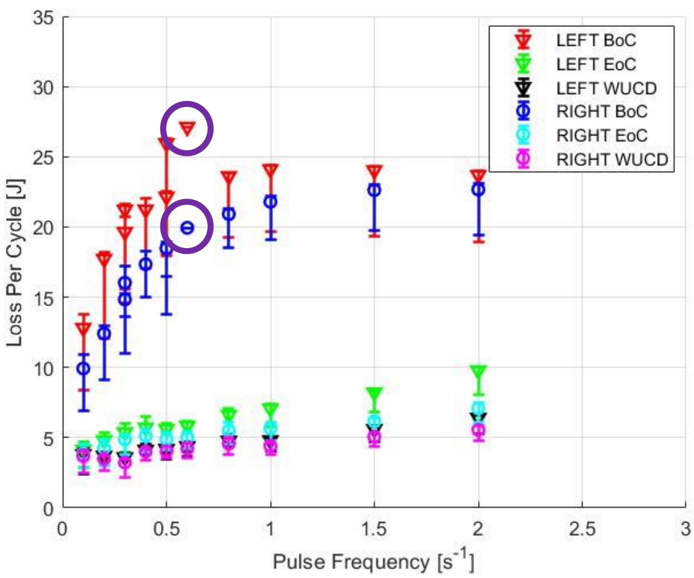

Figure 4.5.1: AC loss measurements results for the two sample legs.

The values of energy deposited relative to the pulse at 0.6 Hz at BoC are marked with purple circles to underline that no measurements were possible with the temperature and pressure sensors far from the location of the inductive coils, because of a loss of signal just after the end of the plateau. Thus, no errorbars can be placed on these measurements.

From the resulting loss curves for the Loss per Cycle, it is noticeable the reduction of the AC losses after EM cycles and WUCD. This is consistent to what expected and to what has been observed in other Nb_3Sn CICC cables ([45], [46], [47]). The AC loss reduction after EM and thermal cycles can be attributed to the increase of inter-strand resistance due to the detachment of the strand-bonding during cyclic loading [45]. Comparing the loss curves for the TF conductor samples, the values of the loss per cycle are close for the two samples, with slightly higher loss values in the TF-A (left leg). After the reduction of the losses with EM cycles, the loss curves after the second thermal WUCD cycle are just slightly lower than the curves at EoC, proving an almost stable energy deposition due to AC losses for the cycled conductor.

For the characterization of the coupling time constant ($n\tau$) and the hysteresis losses, the linear interpolation of the loss curves described in Section 3.5 has been applied up to the pulse frequency of 0.5 Hz. The line interpolations superimposed to the loss curves are shown in Figure 4.5.2.

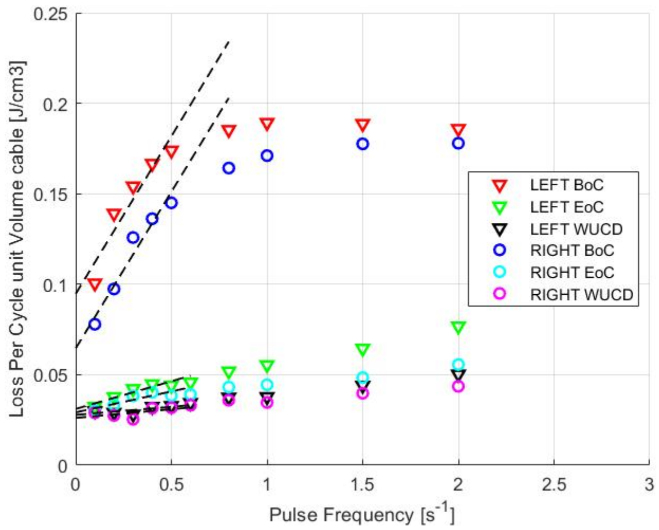

Figure 4.5.2: Results of the Loss per cycle per unit volume for the two sample legs with superimposed linear fits for the computation of the loss contributes.

The obtained values of the coupling time constant and of the hysteresis losses are summarized in Table 11, for the two legs in the different testing conditions.

	Left BoC	**Left EoC**	**Left WUCD**	**Right BoC**	**Right EoC**	**Right WUCD**
$n\tau$ [ms]	123.2	21.6	6.4	122.4	16.4	6.8
P_{Hyst} [J]	12.05	3.96	3.54	8.22	3.72	3.33

Table 11: Results of the n-tau parameter and of the hysteresis losses for the two DTT TF conductor samples.

For the $n\tau$ parameter the obtained values at EoC and after WUCD are much lower than expected, compared to the results of AC characterizations on the ITER Nb_3Sn conductors ([45], [46]), in which orders of hundreds of milliseconds are recorded. For this, a further assessment should be foreseen, applying more refined AC loss analytical models for the estimate of the $n\tau$ parameter.

4.6 MQE tests

The tests of minimum quench energy, as described in Section 3.6 showed some criticalities for the behavior of the TF-B conductor: quench occurred at minimum pulse coil voltage of 140V, even at low testing temperatures (5 K). For this reason, it was not possible to test the minimum quench energy in the TF-A conductor (left leg sample). Although the reliability of the obtained results remains compromised by the unexpected behavior observed, the results from the calorimetry on the calibration run for both the conductor samples are presented in Figure 4.6.1.

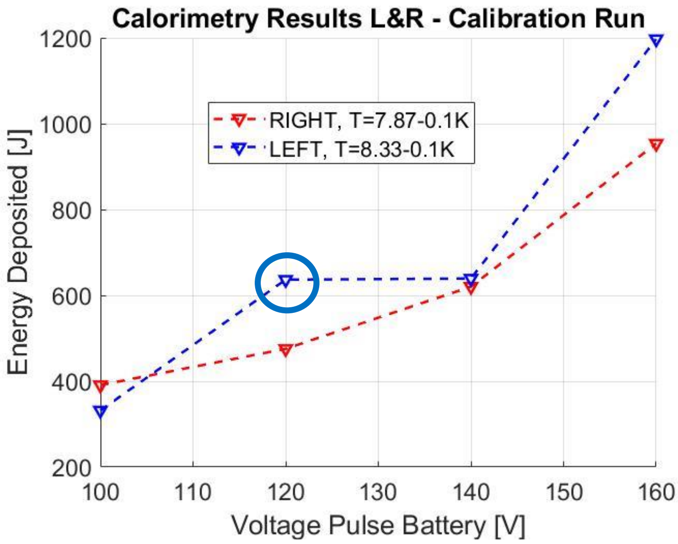

Figure 4.6.1: Calorimetry results as function of the applied voltage on the pulse coils. Blue circle on the Left leg measurement at 120V with the same deposited energy found at 140V.

The calorimetry results for the two leg samples are reported for the comparison on the power deposited from the same fast discharge on the inductive coil. The resulting energy deposited in the left leg sample at 120 V gives a value comparable to the one associated to the pulse at 140 V. Considering that it was applied a linear offset removal on the thermal pulse, the result appears to be unphysical. Also considering the proximity of the other energy values for the two legs, this value at 120 V can be discarded from the analysis, showing a higher deviation with the corresponding value for the right leg and not following the expected increasing trend of the energy deposited as function of the voltage on the pulse battery.

Considering the pulse at 140V as reference minimum voltage at which the quench has been observed in the right leg, it can be determined the corresponding minimum quench energy for the right leg conductor:

$$MQE_R = 620.3 \ J \tag{4.6.1}$$

This value is commonly normalized to the volume of the cable to obtain the value of energy per unit volume:

$$mqe_R = \frac{MQE_R}{V_{cable}} = 4.9 \ \ J/cm^3 \tag{4.6.2}$$

With the volume of the cable computed as:

$$V_{cable} = (N_{strand} + N_{Cu}) A_{strand} L_{coil} / \cos\theta \tag{4.6.3}$$

As already described in Section 3.5.

Conclusions and perspective

In the present work, the experimental qualification of the performance of the first ENEA superconducting cables for the toroidal-field coils of the Divertor Tokamak Test Facility have been performed. The two full-scale, short-length conductor samples with different twist-pitch have been prepared and tested in the SULTAN facility of EPFL-SPC, located at the Paul Scherrer Institute in Villigen, Switzerland. The TF conductor samples preparation and instrumentation procedures in SULTAN have been described. The main performance parameters for a SC magnet were investigated in specific tests according to the ENEA test plan: pressure drop characterization tests, experiments on critical current and current sharing temperature (DC tests), minimum quench energy MQE tests and AC loss measurements. The detailed analyses of the used experimental testing procedures and the analysis and interpretation of the observed phenomena have been reported. The results of the SULTAN test campaign on the TF conductor samples have been critically presented.

Concerning the pressure drop characterization on the TF-B sample, the value of the friction factor at EoC for the nominal mass flow rate (4 g/s) is perfectly captured by the Modified Darcy-Forchheimer correlation, used so far for numerical analysis with the 4C code. The presence of an obstruction in the inlet region of the sample did not allowed measurements at higher mass flow rates, particularly for the run at BoC. The partial recover of the obstruction in the EoC allowed however to obtain significant results at least after EM and thermal cycles.

The current sharing temperature tests showed a minimum T_{cs} of ~6.4 K in the TF-B (right leg) conductor and ~7 K in the TF-A (left leg) at EoC, with *m-values* of 13 and 37 for the TF-B and TF-A respectively. The minimum temperature margin for the TF operation is increased by ~0.4 K in the TF-B and ~1.1 K in the TF-A with respect to the target value: the requirement on the conductor performance is therefore satisfied.

From the critical current measurements, values of 33.8 kA for the TF-B and 36.5 kA for the TF-A have been found at EoC, with values of the *n-index* of ~4-5 and ~12-13 respectively.

From the DC tests results after electromagnetic cycles and WUCDs, a more evident degradation was observed in the TF-B conductor compared to the TF-A sample.

From the measurements of current sharing temperature at different EM loading conditions, it was performed the analysis of the cable strain under different Lorentz forces. Lower values of compressive strain were found for the TF-A sample, with a maximum compressive value of ~ -0.55%. In the TF-B, higher compressive values up to ~ -0.75% were obtained. In both samples the expected linear behavior of the strain with respect to the electromagnetic load was successfully observed.

The MQE tests showed some issues as it was not possible to measure the minimum quench energy in the TF-A. The results of the calorimetry on the TF-B showed a value of minimum quench energy of ~620 J, although for the described issue further assessments are needed to prove the reliability of the result.

The AC loss tests showed losses reduction after cycles, as expected. The effect of the thermal cycles of WUCD have not significantly decreased the loss curves from the values at EoC. The values of the $n\tau$ coupling time constant were much lower than expected, particularly at EoC and after WUCD. For this reason, further assessments are needed. The adoption of more refined AC loss models with less stringent assumptions is envisaged.

This work aimed to the experimental analysis of the results from the SULTAN test campaign on the first DTT TF conductor samples. Future system level analysis on the full TF magnets can be integrated with these experimental results, to better support the verification of the design of the DTT TF magnet system. From the experimental test campaign important results emerged on the performance of two of the proposed designs for the DTT TF.

For the higher temperature margin, lower degradation, and higher *n-values*, the overall best performances are from the TF-A conductor sample. The future design of the DTT TF magnet systems should consider the experimental results observed during the SULTAN test campaign. However, further work will be done. Destructive inspections on the TF-B sample will reveal the origin of the observed flow-obstruction. Further analysis on the MQE tests should be fundamental to understand the unexpected behavior of the right leg, together with more refined analysis of the AC loss measurements, concerning the low values of the $n\tau$. For this, the use of other analytical models or the use of different methods for the assessment of the coupling and hysteresis losses should give a relevant step forward from the analysis presented in this work.

A. Appendix

A.1. Scaling law for superconductors

In superconductors, the behavior of the critical current density is commonly described with a scaling law, $J_c(B, T, \varepsilon)$, as function of the applied magnetic field, temperature, and strain. The procedure to obtain the functional dependencies of the critical current density, so to reconstruct the critical surface, consists in finding a parametrization based on the fit of the experimental measurements on the superconducting strands. Making the useful additional assumption that the dependencies can be factorized, different parametrizations of the scaling law for Nb_3Sn superconducting wires have been made available ([48], [49]). For the characterization of the DTT TF Nb_3Sn wires, the parametrization adopted by ITER-IO for their production [50] has been chosen by ENEA [44]. The analytical expression of the ITER scaling law parametrization for the critical current is:

$$I_c\left(T_{cs}, B_{eff}, \varepsilon_{total}\right) = \frac{C}{B} \cdot s(\varepsilon) \cdot (1 - t^{1.52}) \cdot (1 - t^2) b^p \cdot (1 - b)^q \qquad \text{(A.1.1)}$$

With C a constant $[A \cdot T]$, $s(\varepsilon)$ the strain function, $t = T/T_c(\varepsilon)$ the reduced temperature, $b = B/B_{c2}(\varepsilon)$ the reduced magnetic field, and p, q the pinning-force shape parameters. The semiempirical expressions of the strain function and of the functions $T_c(\varepsilon)$ (critical temperature) and $B_{c2}(\varepsilon)$ (upper critical field) can be found in [51] and [44]. The experimental procedure to obtain the parameters of the scaling law is described in [52]. The fit parameters used in the thesis work presented, are listed in [44].

A.2. Effective magnetic field calculation

For the testing of CICC superconducting cables, to the external magnetic field (the SUTLAN background field), the contributions of the fields generated by the two tested superconducting samples must be considered. The effective magnetic field is the reference single constant value of field representative of the contributions of the background field and of the field generated from the strand self-field distributions on the cable section.

The magnetic field inside the conductor is made up of three superimposed fields:

$$\vec{B}(x,y) = \vec{B}_b + \vec{B}_S(x,y) + \vec{B}_r(x,y) \tag{A.2.1}$$

Where B_b is the SULTAN background field, considered constant in the HFZ, $B_S(x,y)$ is the conductor self-field, generated from the electric current carried by the superconducting strands in the tested leg, and $B_r(x,y)$ the return-field generated by the other conductor leg electrically connected in series with the other leg. For the evaluation of the 2D self-field distributions in the cable section, the analytical formulation based on the Strutt simplification [53] has been used.

For the computation of the effective magnetic field, the procedure described in [54] has been used. The effective field is computed from the iterative inversion of the scaling law for the critical current, finding the single constant value of magnetic field at which the current equates the critical current calculated from the iterative solution of [43]:

$$E_{av} = \frac{1}{A_C}\int_S \left(\frac{J}{J_c(B(x,y),T,\varepsilon)}\right)^n dS = E_c \tag{A.2.2}$$

With E_{av} the average electric field on the cable section, E_c the 10 $\mu V/m$ electric field criterion. By iteratively solving for $E_{av} = E_c$ integrating for the full 2D magnetic field distribution, the critical current value is obtained. From this, the value of the effective magnetic field is obtained by iterative inversion of the scaling law.

Bibliography

[1] [Online]. Available: https://www.dtt-project.it/index.php/about/when.html.

[2] A. D. C. Grassie, The superconducting state, Sussex University Press, 1975.

[3] D. Uglietti, "A review of commercial high temperature superconducting materials for large magnets: from wires and tapes to cables and conductors," *Superconducting Science and Technology,* vol. 32, 2019.

[4] M. Yanwei, "Progress in wire fabrication of iron-based superconductors," *Superconducting Science and Technology,* vol. 25, 2012.

[5] D. Geere, "Cern breaks man-made heat record with ~5.5 trillion degree plasma," *WIRED,* Aug. 2012.

[6] S. Atzeni and J. Meyer-Ter-Vehn, Nuclear fusion reactions, Oxford: Oxford Academic, 2004.

[7] P. Bruzzone, "Superconductivity and fusion energy - the inseparable companions," *Supercond. Sci. and Technol.,* vol. 28, 2014.

[8] M. N. Wilson, Superconducting Magnets, Clarendon Press Oxford, 1983.

[9] [Online]. Available: https://physics.stackexchange.com/questions/333151.

[10] [Online]. Available: https://www.iter.org/proj/inafewlines.

[11] G. Ramogida, "DTT - Technical specification for the supply of superconducting cables for the magnetic system," DTT S.c.a.r.l., 2021.

[12] M. Bombardieri, A. Di Zenobio and R. Righetti, "Technical Report: DTT TF Cu DUmmy - Conductor Hold Point data," ICAS, 2021.

[13] SULTAN-team, "User Specification for Conductor Samples to be Tested in the SULTAN Facility," EPFL - Swiss Plasma Center , 2019.

[14] D. Smathers, et al., "Niobium rod quality and its impact on the production of Nb3Sn strand for the Divertor Tokamak Test Facility toroidal coils," *IOP Conf. Series: Materials Science and Engineering,* vol. 1241, 2022.

[15] P. Park and K. Kim, "Status of Nb3Sn strand development in Korea," *Cryogenics,* vol. 48, pp. 347-353, 2008.

[16] G. Rolando, et al., "Minimizing coupling loss by selection of twist pitch lengths in multi-stage cable-in-conduit conductors," *Superconductor Science and Technology,* vol. 27, 2014.

[17] EPFL-CRPP, "Assembly Procedure for ITER SULTAN Sample," Villigen PSI, 2012.

[18] A. Di Zenobio, L. Muzzi and S. Turtù, "Superconducting conductor sample tests to be performed for DTT coils," DTT project, 2021.

[19] M. Breschi, et al., "Results of the TF conductor performance qualification samples for the ITER project," *Superconducting Science and Technology,* vol. 25, 2012.

[20] L. Muzzi, et al., "The JT-60SA Toroidal-Feld conductor reference sample: Manufacturing and Test Results," *IEEE, Trans. On Appl. Supercond.,* vol. 28, 2010.

[21] L. Muzzi, P. G. M. and A. Di Zenobio, "Pressure drop measurement of the TF qualification conductor sample in SULTAN," Report for JT-60SA, 2009.

[22] L. Savoldi, F. Casella, R. Zanino and R. Bonifetto, "Dynamic modeling of a SHe closed loop with the 4C code," *AIP Conference Proceedings: Advances in Cryogenic Engineering,* vol. 1434, no. 1743-1750, pp. 167-176, 2012.

[23] R. Bonifetto, "DTT TFC Design Description Document," DTT S.c.a.r.l., 2021.

[24] M. Bagnasco, L. Bottura and M. Lewandowska, "Friction Factor correlation for the CICC's based on a porous media analogy," *Cryogenics,* vol. 50, pp. 711-719, 2010.

[25] M. Lewandowska and M. Bagnasco, "Modified friction factor correlation for CICC's based on a porous media analogy," *Cryogenics,* vol. 51, pp. 541-545, 2011.

[26] H. Katheder, "Optimum thermohydraulic operation regime for cable-in-conduit superconductors," *Cryogenics,* vol. 34, pp. 595-598, 1994.

[27] P. Decool, et al., "The JT-60SA TF coils: Experimental check of hydraulic operating conditions," *IEEE Trans. on Appl. Supercond.,* vol. 26, 2016.

[28] L. Bottura, "Cable Stability," in *CERN Indico*, Geneva, Switzerland.

[29] L. G. Dorofeev, A. B. Imenitov and E. Y. Klimenko, "Voltage-current characteristics of type III superconductors," *Cryogenics,* vol. 20, 1980.

[30] F. Laviano, "Lecture on "Measurement of critical currents of superconductors"," in *Course of Nuclear Engineering Lab and Advanced Heat Transfer Problems*, Polytechnic of Turin, 2021.

[31] N. Martovetsky, "Correlation between degradation and broadness of the transition in CICC," *Superconducting Science and Technology,* vol. 26, 2013.

[32] R. Wesche, *E-J and E-T Charakteristik des Testleiters secrets A,* Villigen: Private communication, 2001.

[33] ENEA, "Divertor Tokamak Test Facility - Interim Design Report," ENEA Frascati Research Center, Frascati (Roma), Italy, 2019.

[34] R. Bonifetto, A. Di Zenobio, L. Muzzi, S. Turtù, R. Zanino and A. Zappatore, "Thermal-Hydraulic Analysis of the DTT Toroidal Field Magnets in DC Operation," *IEEE Trans. On Appl. Supercond.,* vol. 30, no. 4, pp. 1-5, 2020.

[35] D. Bessette, ITER project, "Report: procedure for Tcs assessments of the ITER/CS SULTAN samples," 2013.

[36] MATLAB, "R2021a," The MathWorks Inc., 2021.

[37] D. Dew-Hughes, "The critical current of superconductors: an historical review," *Fiz. Nizk. Temp.,* vol. 27, pp. 967-979, 2001.

[38] D. Ciazynski, "Review of Nb3Sn conductors for ITER," *Fusion Engineering and Design,* vol. 82, pp. 488-497, 2007.

[39] R. Bonifetto, Energy Department, Politecnico di Torino, "MATLAB functions for the Helium properties calculation from NIST Standard Reference Database 23: Reference Fluid Thermodynamic," Private communication, Torino, 2012.

[40] E. Lemmon, M. Huber and M. McLinden, "NIST Standard Reference Database 23: Reference Fluid Thermodynamic and Transport Properties-

REFPROP Version 9.0," National Institute of Standards and Technology Standard Reference Data Program, Gaithersburg, 2010.

[41] K. Sedlak, P. Bruzzone, B. Stepanov and V. Corato, "A new test method of AC loss assessment for fusion conductors," *Fusion Engineering and Desing,* vol. 146, pp. 928-931, 2019.

[42] A. M. Campbell, "A general treatment of losses in multifilamentary superconductors," *Cryogenics,* vol. 22, pp. 3-16, 1982.

[43] N. Martovetsky, R. Bonifetto, R. Zanino, L. Savoldi, P. Bruzzone, et al., "Characterization of the ITER CS conductor and projection to the ITER CS performance," *Fusion Engineering and Design,* vol. 124, pp. 1-5, 2017.

[44] G. De Marzi, "Parametrization of the critical surface of the superconducing Nb3Sn wires for the toroidla field coils of DTT.," ENEA FSN-COND, 2022.

[45] K. Sedlak, P. Bruzzone, et al., "Measurements of AC Loss Evolution in ITER TF Conductors," *IEEE Trans. on Appl. Supercond.,* vol. 32, no. 6, pp. 1-3, 2022.

[46] K. A. Yagotintsev, W. A. J. Wessel, et al., "Overview of verification tests on AC loss, contact resistance and mechanical properties of ITER conductors with transverse loading up to 30 000 cycles," *Superconductor Science and Technology,* vol. 32, 2019.

[47] Y. Shi, et al., ""Coupling Loss Characteristics of Nb3Sn CIC Conductor for CFETR CS Model Coil," *IEEE Trans. on Appl. Supercond.,* vol. 27, no. 8, pp. 1-5, 2017.

[48] J. W. Ekin, "Strain scaling law for flux pinning in practical superconductors. Part 1: Basic reletionship and applicatoin to Nb3Sn conductors.," *Cryogenics,* vol. 20, pp. 611-624, 1980.

[49] J. W. Ekin., "Unified scaling law for flux pinning in practical superconductors: I. Separability postulate, raw scaling data and parametrization at moderate strains.," *Supercond. Sci. Technol.,* vol. 23, 2010.

[50] L. Bottura and B. Bordini, "Jc(B,T,e) parametrization for the ITER Nb3Sn production," *IEEE Trans. on Appl. Supercond.,* vol. 19, 2009.

[51] A. Godeke, B. ten Haken, et al., "A general scaling relation for the critical current density in Nb3Sn," *Supercond. Sci. Technol.,* vol. 19, pp. 100-116, 2006.

[52] G. De Marzi, B. Bordini, L. Muzzi, et al., "Magnetic and electromechanical characterization of a high-Jc RRP wire for the HL-LHC MQXF cable," *IEEE Trans. on Appl. Supercond.,* vol. 32, pp. 1-5, 2022.

[53] K. J. Binns, P. J. Lawrenson and C. W. Trowbridge, The analytical and numerical solution of electric and magnetic fields, Chichester, England: John Wiley and Sons, 1992.

[54] R. Wesche, "DC performance, AC loss and transient field stability of five medium size NbTi cable-in-conduit conductors with parametric variations," *Cryogenics,* vol. 45, pp. 755-779, 2005.

[55] [Online]. Available: https://www.researchgate.net/figure/6-Boundaries-that-limit-the-superconductivity_fig3_295912826.

[56] LUVATA. [Online]. Available: https://www.luvata.com/products/superconductors.

[57] I. Yukikazu, "HTS magnets: stability; protection; cryogenics; economics; current stability/protection activities at FBML," *Cryogenics,* vol. 43, 2003.